

# On the nature of Globular and Open Clusters (GOC): a study of M16, M67, M3 & M71 <sup>\*</sup>

Emma Dodd<sup>1</sup>, Harry Baker<sup>1</sup>, Hamish Child<sup>1</sup>, Thomas Harrison<sup>1</sup>,  
Matthew Hodge<sup>1</sup>, Alexander Hackett-Evans<sup>1</sup> & David Sobral<sup>1†</sup>

<sup>1</sup> Department of Physics, Lancaster University, Lancaster, LA1 4YB, UK

Accepted 29 May 2019. Received 23 May 2019; in original form 25 March 2019

## ABSTRACT

A new study of two open clusters, M16 and M67, and two globular clusters, M3 and M71 is presented, exploring data taken with the WFC/INT and the *Hubble Space Telescope* (*HST*) in a variety of broad-band filters. A dedicated, fully functioning reduction pipeline was constructed to reduce the data used in this study. Employing **SExtractor**, photometry is conducted in both  $g$  and  $i$  band filters to obtain Hertzsprung-Russell (HR) diagrams which are fitted with isochrones to determine the average age, distance, metallicity and extinction of each cluster. We find that M16 is  $\approx 2$  kpc away, with a high dust extinction of  $E(B-V) \approx 0.5$ . For M67 the distance was found to be  $\approx 0.7$  kpc and the cluster is less affected by extinction, showing  $E(B-V) \approx 0.2$ . M3 is consistent with being 13 kpc away and it shows little to no extinction. For M71 the distance was found to be  $\sim 3$  kpc and we estimate a moderate extinction of  $E(B-V) \approx 0.25$ . The results of this study highlight the stark contrast between open and globular clusters. We find that M16 and M67 (open clusters) have average ages of  $< 10$  Myrs and 3.5 Gyrs, respectively. Globular clusters are found to be much older with ages of 9.5 Gyrs and 11 Gyrs for M3 and M71, respectively. It was found that open clusters contained stars that are on average more metal-poor, with lower metallicities of  $[Fe/H] \approx -0.8$  to  $[Fe/H] \approx -0.5$ , compared to  $[Fe/H] \approx -0.5$  and  $[Fe/H] \approx 0.05$  for M16 and M67, respectively. Future work could be undertaken to correct for issues found in this study, and investigate/infer the metallicities of the birth clouds.

**Key words:** Open Clusters, Globular Clusters, Clusters, M3, M16, M67, M71.

## 1 INTRODUCTION

The Milky Way formed at least 13 billion years ago (Schlaufman et al. (2018) found the oldest star to be 13.53 billion years old) from Population III stars (Pop III) and the first star clusters. Pop III stars are the theorised, metal free, first generation stars (see Schaerer 2002; Weiss et al. 2000; Gao et al. 2010) for theoretical modelling of such stars, formed from the primordial hydrogen and helium produced in the nucleosynthesis of the Hot Big Bang (e.g. Boesgaard & Steigman 1985; Umemura & Susa 2001). Pop III stars are yet to be observed, despite many studies that have been and currently are being conducted into finding these stars in the Milky Way (e.g. Johnson 2015; Ishiyama et al. 2016) and at high redshift (e.g. Sobral et al. 2015; Sarmiento et al. 2018).

Fusion of hydrogen and helium in the cores of the first stars produced heavier elements (commonly referred to as metals in astrophysics) seen in the present Universe (e.g. Trenti & Shull 2010). Metals enriched the Galaxy when these Pop III stars went supernova so that the following generation of stars, Pop II, formed from these more metal enriched gas clouds (e.g. Trenti & Shull 2010) such that they had higher metallicity (commonly measured as the ratio of Fe abundance over H abundance  $[Fe/H]$ ). The next generation, Pop I, are even more metal rich than Pop II, forming from the remnants of Pop II stars (see Chiosi & Nasi 1974).

The bluer of the Pop I stars are found in the spiral arms of the Milky Way where star formation is still occurring. These stars are found in open clusters, also known as galactic clusters, of which 1537 are known (e.g. Dias et al. 2002). These star clusters are irregular shaped (Dias et al. 2002; Kharchenko et al. 2005b). Open clusters allow us to investigate stellar formation, spiral arm structure and even

<sup>\*</sup> Based on observations made with the INT (I18AN001) and with the NASA/ESA *Hubble Space Telescope* Proposal 6805.

<sup>†</sup> PHYS369 supervisor.

the rotation curve of the Galaxy which can be used in determinations of dark matter halo mass (Friel 1995).

Older Pop II stars are found around the central bulge and in the halo of the Galaxy, some of which reside in globular clusters; dense, approximately spherical grouping of  $10^6$  stars, all gravitationally bound together orbiting a common centre of gravity. These clusters are of scales larger than the solar system, most being found in the halo orbiting the galactic centre (Heggie & Hut 2003). Globular clusters are some of the oldest structures in our Universe, theorised to have formed before the host galaxy itself, acting as building blocks for galaxy formation (e.g. Zocchi 2014).

There are  $\sim 160$  known globular clusters (see e.g. Kharchenko et al. 2005b) in the Milky Way and by studying these clusters a better understanding of how the Galaxy formed can be obtained. Through estimating the cluster's ages one can better constrain the age of our own Galaxy (e.g. Zocchi 2014). These clusters can also be studied to provide constraints on cosmology and by studying the oldest globular clusters in the Milky Way gives a best fit age estimate of  $12.6 \times 10^9$  yrs, with a 95% confidence upper limit of 16 billion years (see Krauss & Chaboyer 2003). The most massive and hence brightest stars in a globular cluster are found in the centre, due to mass segregation. Mass segregation (see King et al. 1995; Baumgardt et al. 2008) is a process in which globular clusters collect their high mass stars in the centre and the lighter ones orbit at greater speeds at larger radii. This makes resolving the dense inner regions of these clusters difficult and practically impossible until the advent of CCD photometry.

Stars form from an initial mass, typically in clusters (see Bonnell & Davies (1998) for a study of this), determined by the Jean's mass (Padmanabhan 2000). The Initial Mass Function (IMF) will determine the characteristics of the star and its evolution. After a star has formed, it enters its 'main sequence' existence, during which it will fuse hydrogen into helium, producing enough outward pressure to be able to prevent its collapse due to gravity and is therefore stable. The luminosity of the star is determined by its mass  $(\frac{L}{L_{(\odot)}}) \propto (\frac{M}{M_{(\odot)}})^4$ , and as stars are treated as black bodies, their surface temperature is related to luminosity by  $(\frac{L}{L_{(\odot)}}) \propto (\frac{T}{T_{(\odot)}})^4$ , thus creating a relation between the mass of a star and its surface (or effective) temperature (Padmanabhan 2000). These are divided into spectral classes, from O being the most massive, luminous and blue hot main sequence stars to M being the lightest, dimmest and coldest red main sequence stars (Padmanabhan 2000).

The ratio between temperature and mass of stars can be exploited with a Hertzsprung Russell (HR) diagram. These diagrams are constructed by plotting temperature (which as mentioned relates to spectral class; Bohm-Vitense 1981) against absolute magnitude for a sample of stars. There are four major regions where stars lie on the diagram; most stars lie along the main sequence. This region is densely populated, being a region of stellar stability, a star spends most of its lifetime on the main sequence burning hydrogen into helium via nuclear fusion. Eventually, a star will exhaust its supply of hydrogen, and so will evolve onto a different region of the HR diagram.

The three remaining regions on HR diagrams are also regions of stellar stability, but for shorter timescales than

the main sequence. These are the red giants, super (blue) giants, and white dwarfs. Which branch of evolution a star may take depends on its initial main sequence mass (Iben Jr 1974). Within clusters, the O,B then A stars will be the first to progress from the main sequence onto the super giant branch, and eventually explode in supernovae as they are hotter and thus exhaust their fuel more rapidly (Salpeter 1955). On longer time scales, less massive stars will progress onto the red giant branch after exhausting their fuel (Tayler 1981). Over time, the bluest stars will 'die off' first, then the more yellow stars and so on until only the red stars remain. This will be seen on a HR diagram by a lack of the top ends of the main sequence, and the turn-off point will be shifted lower on the main sequence, allowing one to determine the age of a cluster (Charlot & Bruzual 1991). The main sequence turns off onto the red giant branch (RGB). Stars that have evolved away from the RGB then form the horizontal branch. These stars have helium burning cores, they are bluer than RGB stars and of lower magnitude (brighter) than main sequence stars.

This study used HR diagrams to analyse the selected data, the selection of which to use in our investigation is discussed in Section 2. A 'pipeline' was then constructed to process our images selected into useful data that could be analysed to investigate the characteristics of our clusters. In Section 3 we present the data reduction. Section 4.1 discusses the determination of zero-points and magnitudes. In Section 4.2 we present the HR diagrams. In Section 4.3 we use isochrone fitting to the HR diagrams and obtain the best physical parameters. Our results are presented in Section 5, they discussed in Section 6 and we present the conclusions of our work in Section 7.

## 2 SAMPLE AND DATA

### 2.1 The Sample of Open and Globular Clusters

The clusters that will be studied are two open clusters: M16 and M67 (Table 2), and two globular clusters: M3 and M71 (Table 2), all of which have been studied extensively (see Arp & Hartwick 1971; Janes & Demarque 1983; Hillenbrand et al. 1993; J. Tripicco et al. 1993; Sandage & Cacciari 1990; Chieffi & Straniero 1989) and Table 3, allowing us to compare our results to previous studies.

The data for these four clusters was obtained during 14-19 May 2018, at the Isaac Newton Telescope (INT) in La Palma. This data was ideal for the open clusters M16 and M67 as the stars within these clusters are not associated with high density regions that over-crowded cameras, however for the globular clusters, M3 and M71, the resolution of the centre of the cluster was not ideal. For this the Hubble Space Telescope (*HST*) was used as it is able to resolve the centre of these clusters better than the INT. The data for M3 here was obtained from an observing run in 2003 by *HST*, from an investigation into blue stragglers in the centre of M3 (*HST* proposal 6805; Ferraro et al. 2003). For M71 we used the INT data and sample stars from around the centre by placing a mask over the centre, further explained in section 4.1.3.

Lists of the targets selected and the filters can be found in Table 4, with the properties of the filters listed in Table 1.

Filter Band	$\lambda$ (Å)	FWHM (Å)
g	4846	1285
i	7743	1519
[OIII]	5008	100
StromgrenV	4110	150
F814W / WFPC2 Wide I	8024	1536
F555W / WFPC2 V	5308	1562

**Table 1.** Filter bands used in this study. The g,i, [OIII] and Stromgren V specifications come from the ING (ING 2018a).

### 2.1.1 Open Cluster: Messier 16

M16 is famous for the Pillars of Creation, it is believed to contain around 8,100 stars (Kuhn et al. 2015). The cluster also features the Sagittarius Arm, where high mass stars ( $\sim 80M_{\odot}$ ) are currently forming (Nishimura et al. 2017).

Due to the clusters youth it features no red giants and therefore no turn-off point (Selim et al. 2016), which is important to see how the cluster’s individual stars have evolved off the main sequence, allowing the cluster’s age estimated. Since none of the stars in the cluster have evolved off the main sequence, previous studies have determined M16 must be  $\leq 10$ Myr (Selim et al. 2016) as none of the high mass stars have evolved to the red giant branch. One of the most recent studies into the cluster (see Selim et al. 2016) made colour magnitude diagrams from CCD images. By fitting isochrones for pre-main sequence stars and using 2MASS data, the study found a distance =  $2.2 \pm 0.21$  kpc, age = 3.6 Myr and metallicity  $[\text{Fe}/\text{H}] = 0.019$ . For further past results see Table 3.

### 2.1.2 Open Cluster: Messier 67

With a radius of 10 light years, M67 is the smallest cluster in our sample, and according to Sanders (1977) it contains over 500 stars. M67 was once thought to be the Sun’s parent cluster due to the presence over 100 Sun-like stars in the cluster, though recent simulations have deemed this unlikely (e.g. Pichardo et al. 2012).

By analysing the spectral lines of iron, the metallicity of M67 was found to be  $[\text{Fe}/\text{H}] = 0.06$  (VandenBerg et al. 2014). The same study used the turn off point of their fitted isochrone, created by simulated data, to determine the age of the cluster to be 4.3 billion years. Zapata (2016) found a value for distance of  $0.83 \pm 0.06$ kpc. For further past results see Table 3.

### 2.1.3 Globular Cluster: Messier 3

M3 (or NGC 5272) is an ideal cluster to study a large sample of Pop II stars (see Ferraro et al. 1997). M3 is a nearby globular cluster and past results find low values for the clusters extinction, (e.g. Ferraro et al. 1997). This work also studied the inner regions of M3 using photometry of Hubble images and found  $E(B-V) = 0.01$ .

The prediction for the age of M3 has changed over the years, back when globular clusters were first being studied this way, Haselgrove & Hoyle (1956) gave the best age estimate at the time, but it is now thought the cluster is approximately twice this age. Paez et al. (1990) found a distance of  $9.51^{+0.18}_{-0.17}$ kpc to the cluster using CCD photometry

and constructing a colour magnitude diagram similar to the methods implemented in this study.

Another widely measured parameter of this cluster is  $[\text{Fe}/\text{H}]$ . Kraft et al. (1992) found  $[\text{Fe}/\text{H}] = -1.47 \pm 0.01$  from seven stars within the cluster and also found no strong evidence for variations from star to star in the  $[\text{Fe}/\text{H}]$  value. Chieffi & Straniero (1989) measured and the  $[\text{Fe}/\text{H}]$  to be  $-1.4$  which is then used to consider three different ages for M3; (14, 16, 18)  $\times 10^9$  years. They then make a best fit to the main sequence, turn off point, and red giant branch using the distance and extinction of M3 as free parameters. They find the best fit comes from an age ranging between  $16 - 18 \times 10^9$  years with  $[\text{Fe}/\text{H}]$  set and the distance and extinction values found are summarised in Table 3.

### 2.1.4 Globular Cluster: Messier 71

M71, or NGC 6838, is a Globular Cluster found in the Sagitta constellation. It has been observed over many years, after being first discovered in 1745. Over this time its age, distance, metallicity and extinction have been measured by multiple different methods. Some of these results are quoted in Table 3.

Using ground based images and creating isochrones on colour-magnitude diagrams, Cohen et al. (2001) found an age of  $(12 \pm 1)$  Gyr. The same study found the cluster to be at a distance of 4 kpc and have a  $[\text{Fe}/\text{H}]$  metallicity value of  $-0.78$  (Cecco et al. 2015). Comparing the (B-V) value to the magnitude on the colour magnitude diagram can be used to determine the extinction of the cluster, this method was used to find a value of 0.25.

## 2.2 Hubble Space Telescope

The Hubble Space Telescope is a telescope launched into low earth orbit in 1990 by NASA, with contributions from ESA. On board the *HST* currently is the Wide Field Camera 3, however for the purposes of this investigation data from its predecessor, the Wide Field Planetary Camera 2 was used. The Wide Field and Planetary Camera 2 was decommissioned in 2009 and held many of the same properties as the WFC3, viewing in the UV, visible and near infrared, 120nm – 1000nm (Dressel 2008). During an observing run for a paper in 2003, *Investigating Blue stragglers in the centre of M3* (Ferraro et al. 2003, *HST* Proposal 6805), images of the centre of M3 were taken in the F555W and F814W filters. These images are used in this study. The images taken with the WFPC2 are in the wide-band filter, useful to this investigation as it allows a larger variety of catalogues to be used.

This is because the wide-band views objects through a larger range of wavelengths, rather than through specific narrow-band channels, allowing more flux to be captured by the camera so more objects can be viewed and compared to existing catalogues.

## 2.3 WFC/INT Observations

During the observing run at INT in La Palma May 2018, our clusters were observed across two nights with the open clusters, M67 and M16, being observed on May 14 2018 and

Cluster	RA	Dec	$m_g$	Colour	No. of Stars
M16	18:18:48.70 <sup>6</sup>	-13:48:24 <sup>7</sup>	6.0 <sup>9</sup>	0.15 <sup>11</sup>	8100 <sup>8</sup>
M67	8:51:25.1 <sup>6</sup>	11:48:00 <sup>7</sup>	6.1 <sup>10</sup>	1.664 <sup>12</sup>	$\sim 500^8$
M3	13:42:11.62 <sup>1</sup>	28:22:38.2 <sup>1</sup>	$7.071 \pm 0.002^2$	0.93 <sup>4</sup>	$\sim 500,000^3$
M71	19:53:46.49 <sup>4</sup>	+18:46:45.1 <sup>4</sup>	$7.973 \pm 0.039^2$	1.36 <sup>4</sup>	$>20,000^5$

**Table 2.** Astrometry and general characteristics of clusters selected. [1]:(Goldsbury et al. 2010), [2]:(Vanderbeke et al. 2013), [3]:<https://www.messier-objects.com/messier-3/>, [4]:(Harris 1996) in V-I colour index, [5]:<https://www.messier-objects.com/messier-71/> [6]:(Kharchenko et al. 2005a), [7]:(Wu et al. 2009), [8]:(Sanders 1977), [9]:<https://www.messier-objects.com/messier-16-eagle-nebula/> apparent magnitude, [10]:<https://www.messier-objects.com/messier-67-king-cobra-cluster/> apparent magnitude, [11]: (Guarcello et al. 2010) in V-I colour index, [12]: (Önehag et al. 2011) in V-I colour index.

Study	Age (yr)	Distance (kpc)	[Fe/H]	E(B-V)
<b>M16</b>				
(Nishimura et al. 2017)	-	1.8	-	-
(Bonatto et al. 2006)	$(1.3 \pm 0.3) \times 10^6$	$1.8 \pm 0.5$	-	0.8
(Selim et al. 2016)	$3.6 \times 10^6$	$2.2 \pm 0.21$	0.019	$0.31 \pm 0.02^1$ $0.53 \pm 0.04^2$
(Hillenbrand et al. 1993)	$2 \times 10^6$	2	-	0.4 $\sim$ 1.8
(Guarcello et al. 2009)	$(2 \sim 3) \times 10^6$	1.4 $\sim$ 1.7	-	-
<b>M67</b>				
(J. Tripicco et al. 1993)	$4.6 \times 10^9$	0.8 – 0.9	$0.00 \pm 0.06$	$0.041 \pm 0.004$
(Taylor & Joner 2005)	$5 \times 10^9$	0.813	-	0.032
(Sato & Audouze 2012)	-	-	-	0.046
(VandenBerg et al. 2014)	$4.300 \times 10^9$	-	0.04	-
(Oliveira et al. 2013)	-	-	0.06	$0.03 \pm 0.003$
(Önehag et al. 2011)	$(4.2 \pm 1.6) \times 10^9$	0.790	0.03	0.04
(Zapata 2016)	$(3.72 \pm 0.19) \times 10^9$	-	$0.023 \pm 0.015$	-
(Sarajedini et al. 2009)	$3.5 \times 10^9 - 4.0 \times 10^9$	$0.830 \pm 0.060$	$0.0 \pm 0.3$	$0.03 \pm 0.03$
(Kai-ping et al. 1993)	$5 \times 10^9$	-	$0.009 \pm 0.009$	$0.041 \pm 0.004$
(Kai-ping et al. 1993)	$5 \times 10^9$	$0.843 \pm 0.138$	-	-
<b>M3</b>				
(Watkins & Van der Marel 2017)	-	$4.44^{+∞}_{-2.5}$	-	-
(Cudworth 1979)	-	$9.6 \pm 2.6$	-	-
(Sandage & Cacciari 1990)	$18.6 \times 10^9$	$9.16^{+0.43}_{-0.41}$	-1.66	0.01
(Paez et al. 1990)	-	$9.51^{+0.18}_{-0.17}$	-	-
(Ferraro et al. 1999)	-	$10.05^{+0.97}_{-0.88}$	-	-
(Marconi et al. 2003)	-	$10.33 \pm 0.24$	-	-
(Kraft et al. 1992)	-	-	$-1.47 \pm 0.01$	-
(Carretta & Gratton 1997)	-	-	$-1.34 \pm 0.02$	-
(Chieffi & Straniero 1989)	$14 \times 10^9$	15.10	-	0.03
(Chieffi & Straniero 1989)	$16 \times 10^9$	14.95	-1.4	0.00
(Chieffi & Straniero 1989)	$18 \times 10^9$	14.90	-	0.00
(Harris & Racine 1979)	-	15.00	-	0.01
(Gratton 1985)	-	14.96	-	0.01
(Thassana & Maithong 2017)	$\sim 11.1 \times 10^9$	10.42	-	-
(Ferraro et al. 1997)	-	-	-	0.01
(Haselgrove & Hoyle 1956)	$\sim 6 \times 10^9$	-	-	-
<b>M71</b>				
(Cecco et al. 2014)	$12.1 \times 10^9$	-	-	-
(Cohen et al. 2001)	$12 \times 10^9$	3.900	-0.7	0.25
(J. Davidge & A. Simons 1994)	$(13.5 \pm 2) \times 10^9$	-	-0.65	0.28
(Salaris & Cassisi 1997)	-	3.800	-0.8	0.28
(An 2008)	-	-	-0.73	0.25
(An 2008)	-	-	-0.81	0.32
(Cecco et al. 2015)	$(12 \pm 1) \times 10^9$	4	-0.78	-
(Arp & Hartwick 1971)	$7.6 \times 10^9$	4.11	$-0.3 \pm 0.2$	0.31
(Yim et al. 2004)	-	$4.92 \pm 0.17$	-	-
(G. Cohen 1980)	-	-	-1.27	-
(Zinn 1985)	-	4.51	-0.58	0.27
(Heasley & Christian 1991)	$16 \times 10^9$	-	-	-
(Hodder et al. 1992)	$(14 \sim 16) \times 10^9$	-	-	-
(Janes & Demarque 1983)	$14.45 \times 10^9$	5.13	-0.7	0.28
(Harris 1996)	-	4	-0.78	0.25

**Table 3.** Characteristics of our clusters found by previous studies. [1]: E(J-H) used instead. [2]: E(V-I) used instead.

the globular clusters, M3 and M71, on May 15 2018 (see Table 4). The seeing on the first night of observations was  $1'' - 1.3''$  with thin clouds. On the second night the seeing was poorer throughout the night, varying between  $2'' - 3''$ .

As well as the target science images, flats and biases were also taken on the observing night. Biases were taken by reading the CCD not exposed to any light. This represents the noise caused by the amplifiers of the CCD. Since these are taken without light exposure, the filter on the CCD does not effect the bias and so they only need to be taken in one filter. Flats were taken by exposing the CCD to uniform brightness, with the dome open during twilight. Flats were taken for each filter that was observed in the clusters.

### 3 DATA REDUCTION

The ‘GOC pipeline’ was developed to process the raw images from the INT, into reduced images that can be used to conduct photometry. The easiest way to achieve this is using a Python script. Python 3.7 was chosen and the *Astropy* package which contains many useful methods to handle FITS files. A more indepth overview of how the GOC Pipeline was made and the issues that were faced is explained in Appendix A. The script developed first takes the raw images from the INT, splitting them into separate FITS files for each CCD of the WFC. The main header must be preserved as it contains the important information about the image’s location in the sky which is needed later in Stage 2 to match to reference catalogues, so each of these FITS files has the main header appended to them. Then, bias subtraction and flat division is performed on the science images. The images are then astrometrically corrected. Finally, the frame from each CCD is combined together to form one image for a cluster in a filter band.

#### 3.1 Image Processing

To remove electronic noise from the raw images and correct for the response, (shown in Figure 1), the level bias must be subtracted from the science images, and then divided by  $F / \langle F \rangle$ , where  $F$  is the flat.

The script begins by combining all the bias files taken on the observing night of the science image and finds the median of these biases, the ‘total bias’.

All the apparent flats taken in the same filter, on the same observing night as the science image, are then combined together by the script to create a ‘total flat’. A flat is used by the pipeline script based on the median count value. If the median is lower than 16000 then it is not illuminated enough, therefore there are not enough statistics to relate photon capture to flux, and above 30000 the response is possibly too saturated.

The total flat has to be normalised, which is done by dividing it by its own median value. Therefore, the image reduction calculation is as shown below in Equation 1

$$I_{\text{reduced}} = \frac{I_{\text{raw}} - B_{\text{total}}}{F_{\text{total}} / \langle F_{\text{total}} \rangle} \quad (1)$$

where  $I$  is the science image,  $B$  the bias and  $F$  the flat field. An example of such a reduction is seen in Figure 2, the reduced form of the image of M16 seen in Figure 1.



**Figure 1.** Raw image of M16 from CCD4 of the INT WFC, taken in the  $i$  filter on 14<sup>th</sup> May 2018. The famous ‘Pillars of Creation’ can be seen centred in M16. The defects introduced into the image can be seen in the image, for example, the vertical white line on the left and the general ‘fuzziness’ of the image.

#### 3.2 Astronomy Solutions

The reduced images are not useful without correct R.A. and Dec. co-ordinates within their headers. The FITS header contains information about the image including the observatory, date, filter, target and other important parameters such as pixel scale. The INT produces images with incorrect R.A. & Dec., so they have to be corrected by a re-calibration factor by the pipeline script. This was done by implementing and adapting code from this previous study that used INT images (see Sobral et al. 2016).

With corrected headers that gave R.A. Dec. co-ordinates that located the image to roughly the correct part of the sky, within  $10''$ , the next step was to astrometrically calibrate the images to fix them onto the exact part of the sky they are meant to represent. SCAMP (Bertin 2006) is implemented to achieve this. It first needs to use another piece of software called SExtractor (discussed further in Section

Cluster	INT Filters	Date	Seeing (")	Exposure Time in g	Exposure Time in i
M16	g, i, Stromgren V,OIII	14/05/18	1.0-1.3	10	10
M67	g, i	14/05/18	1.0-1.3	15	15
M3	g,i,StromgrenV	15/05/18	2.0-3.0	4	4
M71	g,i,StromgrenV	15/05/18	2.0-3.0	13	8

**Table 4.** Information on the different filters (specifications of which can be found in Table 1), atmospheric conditions and exposure times of the clusters selected observed with the INT.



**Figure 2.** The reduced image of M16 seen in Figure 1.

4.1) to produce catalogues of sources in our images that SCAMP can read. SCAMP produces a catalogue with the needed corrections to our images, which can then be implemented by SWARP.

### 3.3 Stacking and Final Images

SWARP is a further piece of software that performs the corrections recommended by SCAMP onto our images and can combine FITS files together to produce a mosaic image.

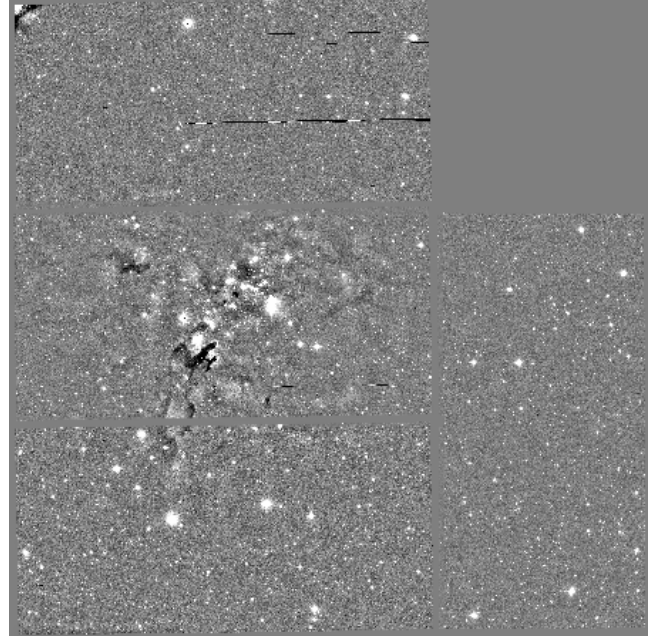


**Figure 3.** Co-added image of M16 in the i band filter taken by the WFC INT on the 14<sup>th</sup> May 2018. There are still defects present, such as bad pixels in the top-left and there are gaps between CCD frames. These issues are overcome in Section 4.1.

The pipeline script uses SWARP to produce a FITS file with its astrometric solution for our reduced images based on the catalogue produced by SCAMP, detailed in Section 3.2. These images have been transformed such that each source has the correct R.A. Dec. co-ordinates so that SWARP can combine the 4 CCD images together, and that SExtractor can correctly match sources to a reference catalogue in Stage 2.

Finally, the corrected images from each CCD could now be combined together using SWARP, to produce a final, reduced image from the INT WFC, with corrected R.A. Dec. and reduced distortions and noise, for a specific cluster in a specific filter. An example of this can be seen for M16 in Figure 3. This process was carried out for all 4 clusters with the various filters chosen, as detailed in Table 4 in Section 2.

These images can then be passed to Stage 2. An RGB image of the cluster can also be produced by using 3 filters, which more serves as a visual demonstration of our image reduction, examples of which can be found in Figure 4.

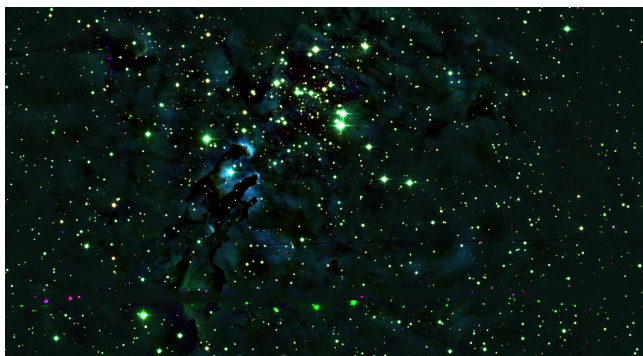


**Figure 4.** False colour image of Messier 16, compiled with INT images in g, i and StromgrenV filters reduced by the GOC Pipeline (see Table 1 in Section 2.1 for filter specifications).

## 4 METHODOLOGY

### 4.1 Producing Catalogues

#### 4.1.1 Determining the FWHM of our images

The FWHM, a consequence of atmospheric seeing, is a measurement of the smallest point source that can be imaged and can be used to quantify the quality of an image. Using an aperture the size of the FWHM for that image will give a source with flux 68% of the true flux. The higher the atmospheric seeing on the night of observations then the higher this FWHM value, and so the stars in the image are already extended by this amount and appear fainter.

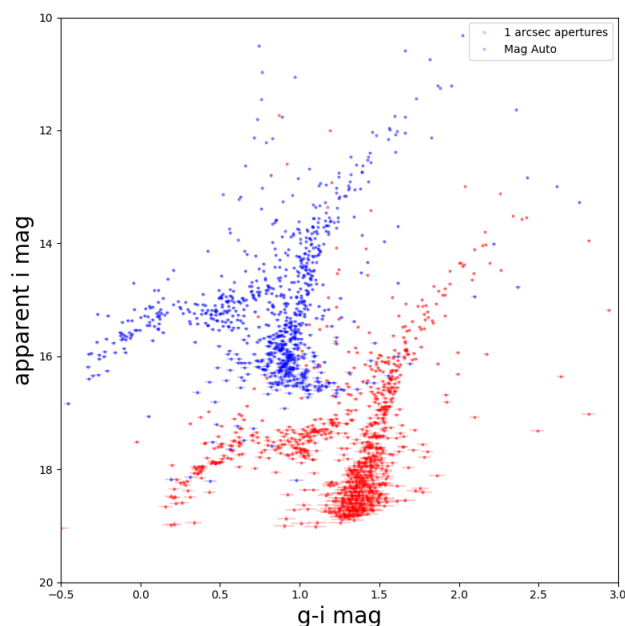
There is a need to quantify this for the cluster in all different filters used to make sure that the seeing did not change drastically between observations in the two filters, if so this will give unreliable colour estimates meaning only images of the same quality can be compared.

Table 5 shows the quantitative effects of atmospheric seeing on our images and the size of the apertures that need to be used as a consequence of this. Mag-Auto is the magnitude that **SExtractor** predicts to be the full magnitude value for a source by measuring the flux for the whole source, looking at how far a source extends and where this flux stops. This is the best estimate for a stars total magnitude and is the brightest of the magnitudes calculated by **SExtractor** but also the magnitude with highest error; larger aperture, more noise.

There is a difference in seeing between the two observing nights with the INT, shown in Table 4. The open clusters were observed on the night with lower seeing and globular on the following night, with higher seeing, and thus the open clusters have FWHM values smaller than the globular, and these images are of higher quality (see Table 5).

#### 4.1.2 Finding the Zero point

Source-Extractor (**SExtractor** Bertin & Arnouts 1996) is a Python based software which can be used to identify and measure all sources in an astronomical image to produce a catalogue of stars. In order to calculate magnitudes from our images, as described in Section 4.1.3, first the zero point had to be determined from our images and then this value inputted into the Python script to execute **SExtractor**.



**Figure 5.** Colour magnitude diagram of INT data for M3 using 1'' apertures and Mag Auto apertures to illustrate the difference between the two. Using apertures smaller than the FWHM value for the image does not give the whole flux and results in stars appearing fainter than their true values.

Cluster	Filter	FWHM (")	Aperture Used
M16	g	1.413	Mag-Auto
	i	1.485	Mag-Auto
	g	2.3883	Mag-Auto
M3	i	2.053	Mag-Auto
	F814W	0.22	1''
	F555W	0.16	1''
M67	g	1.92	Mag-Auto
	i	2.42	Mag-Auto
M71	g	2.99	Mag-Auto
	i	2.83	Mag-Auto

**Table 5.** List of FWHM values for the images of each cluster in each filter used. This value gives a quantitative value for the quality of the image and represents the smallest size point source that can be resolved.

First, we ran **SExtractor** on our images with the zero point of the images set to zero. This produced a catalogue which could then be matched with a catalogue of known magnitudes, see Table 7, using **TOPCAT**, a graphical plotting and reference catalogue finding software (Taylor 2013).

Then we found the difference of each **SExtractor** measured magnitude from our image to the catalogue magnitude, and plotted a histogram of this difference. From this the zero point was found for each of our images by calculating the median. It is possible to get a simple estimate of the error on the ZP from the distribution of this histogram. A small change in magnitude when determining the zero point has a significant impact on our catalogue and this is why the median of the magnitude difference is used as our measurement of the zero point, since this should not be affected

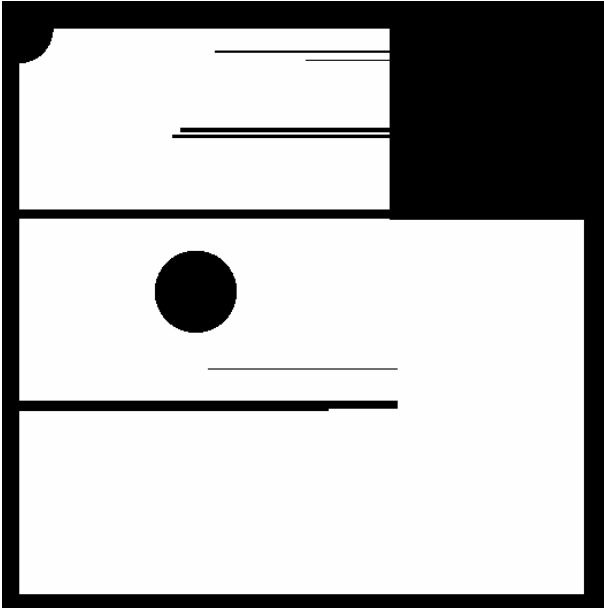


**Figure 6.** Mask produced in order to mask bad pixels and gaps between the CCD's of INT image of M3.

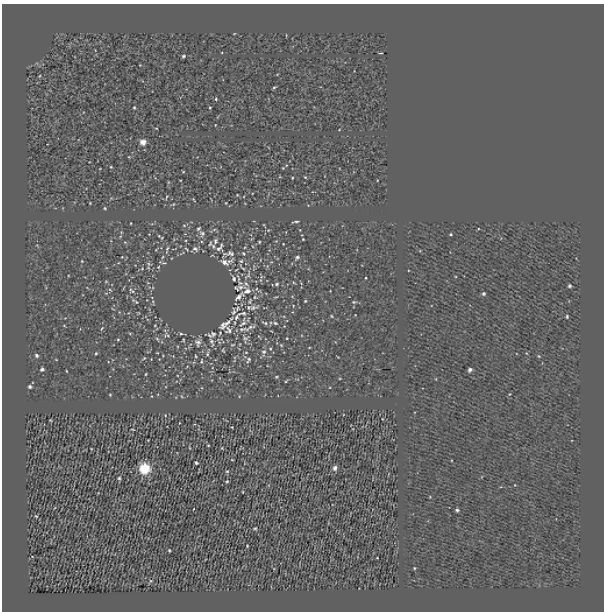


**Figure 7.** Masked and reduced version of INT image of M3 in g band.

by outliers like the average of this difference in magnitude would be.

#### 4.1.3 Running SExtractor

Before running **SExtractor** masks had been produced that can be used to ignore regions of bad pixels in an image. By setting all the bad pixels to have a value of zero and all the good pixels, to a value of one, a mask could be created. An example of one of these masks is Figure 6 and of the masked image of M3, Figure 7.

Running initial INT images with **SExtractor** revealed

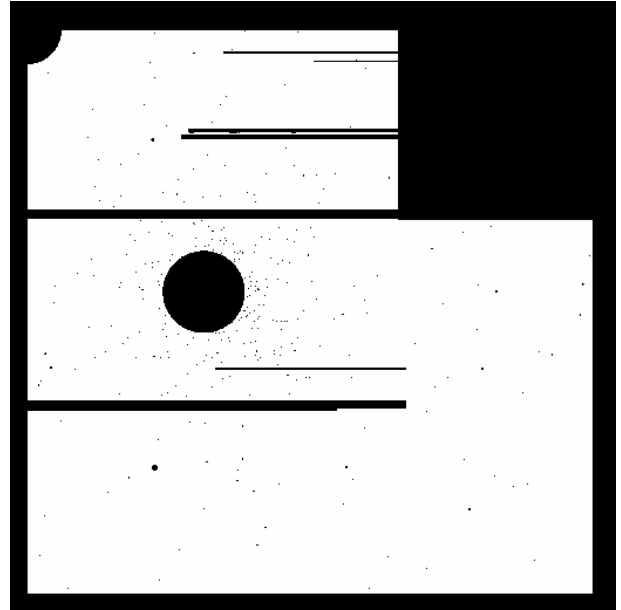


**Figure 8.** Segmentation map of M3 INT image which can be used such that apertures for measuring noise are only placed in background regions of the science image, where the segmentation map has a value of one which corresponds to the white regions in this image.

lots of sources in the gaps between the CCDs, masks are therefore needed to cover redundant parts of the raw image caused by gaps between CCDs. These gaps are the result of the co-adding of the CCD frames performed by **SWARP** in the image reduction, detailed in Section 3.3. Noisy pixels are formed in these gaps which can be recognised as stars by **SExtractor** in the reduced INT images. We reduced the amount of falsely identified sources that were due to noise or bad pixels, by providing **SExtractor** with a mask that defines regions of the image for **SExtractor** to ignore.

#### 4.1.4 Measuring Noise

The errors determined automatically by **SExtractor** are optimistic, and as such they can be used as a lower limit. However, it was able to determine a more realistic error on our magnitudes by measuring the noise in the images. This was measured using a script that places random apertures across the background of the image, the background being the areas of the images where there are no sources. When running **SExtractor** a FITS file was produced that contains the positions of all sources in the catalogue. In this image all the pixels that do not correspond to a source have a value of zero and the sources have the original count value from the observation image. This image is transformed into a segmentation map in which the sources and bad pixels have a value of zero but the remaining areas have a value of one. An example of the segmentation map produced for our INT image of M3 is shown in Figure 8.

The noise is measured globally across the image by placing apertures in random positions across the background of this image, regions where the segmentation map has a value of one. The noise was measured using three different sized apertures; 1", 2" and 3", the same sizes that **SExtractor**

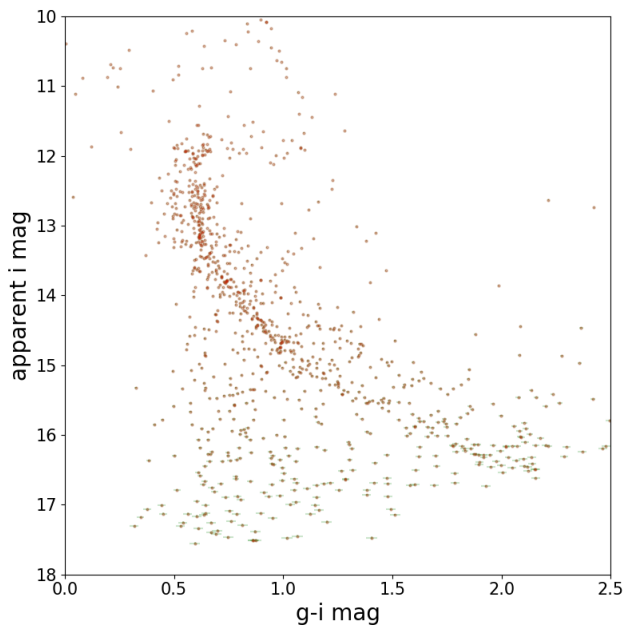


**Figure 9.** Colour-Magnitude plot for M67 using catalogues extracted from the INT images in the g and i filters.

had to measure. This gave us three values for the noise for the different sized apertures measured in counts, where the noise is quantified as the standard deviation of the random apertures of the same size, across the image. Larger apertures contain more flux, has a higher count and thus a larger error. Noise was converted into magnitudes for each source using the individual sources count value,  $c$ , and the global noise of the image,  $\sigma$ , using Equation 2 as the upper error and Equation 3 as the lower error. Taking the error on each source to then be  $\pm \frac{A+B}{2}$ .

$$A = 2.5 \log_{10}(c + \sigma) - 2.5 \log_{10}(c) \quad (2)$$

$$B = 2.5 \log_{10}(c) - 2.5 \log_{10}(c - \sigma) \quad (3)$$

## 4.2 Producing HR diagrams

Once our final catalogues for each cluster had been obtained, explained in Section 4.1 HR diagrams could be produced. When producing colour magnitude diagrams like with like filters are compared as only images of the same image quality can be compared to get reliable results. Here our HR diagram for M67 produced from our INT data in the g and i bands is presented, Figure 9. The main sequence and turn off point can clearly be identified in this data and proved useful when fitting isochrones to our diagrams, discussed in Section 4.3.

### 4.2.1 Radius Cut

The INT images of the globular clusters show the cluster as a whole with the central bulge only taking up a small fraction of the image, as can be seen in Figure 10.

In order to refine our catalogues, the boundary of the

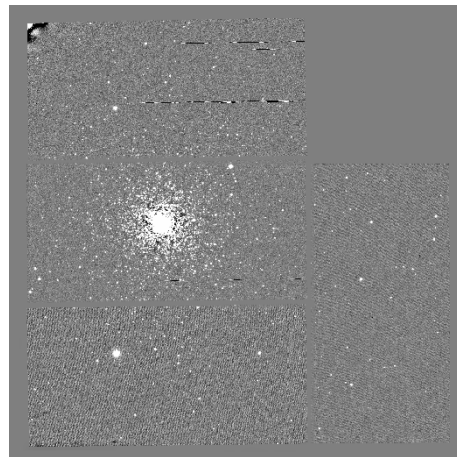


**Figure 10.** Reduced INT image of M3 in g band.

cluster was determined and this radius was used to cut out stars that were believed to not be cluster members. The simple approach taken was to plot the colour magnitude diagram for the cluster while changing the radius cut off to smaller and smaller values to see how the structures in the diagram changes. Cluster stars should lie along the main sequence, where as foreground and background stars will be offset from this due to being at a different distance from the observer, and so it could be used to estimate the radius of our globular clusters. Figure 12 shows how the colour magnitude diagram of M3 changes when the sample is cut down according to the radius and only include sources encompassed in a radius of 0.1 deg, as illustrated in Figure 11. The main structure in the colour magnitude diagram, Figure 12, does not change as the radius changes; clear branches, red giant and horizontal branches can be seen and will be discussed in more detail in Section 6.

## 4.3 Isochrone Plotting and Analysis

Our HR diagrams show the typical regions and structure expected, such as the main sequence and turn-off points onto branches that were mentioned in Section 1. In order to analyse these diagrams to produce quantitative results, the method used in this investigation is fitting the data with isochrones which are curves on the Hertzsprung-Russell diagram that represent, in stellar evolution, a population of stars that have the same age, distance from the observer and metallicity.

### 4.3.1 Implementing Dartmouth Isochrones

In order to analyse the produced HR diagrams, isochrones can be fitted onto the HRDs and the data compared with theory to find values for distance, age, metallicity and extinction.

A Python based ‘isochrone’ package was used to import the required libraries. This package has an interface with the Dartmouth model isochrones (Dotter et al. 2008) which can be downloaded, and then called in for the filter bands used in that particular HRD. A model then can be produced to plot an isochrone over the colour-magnitude diagram using predicted values for: distance, age, metallicity and colour

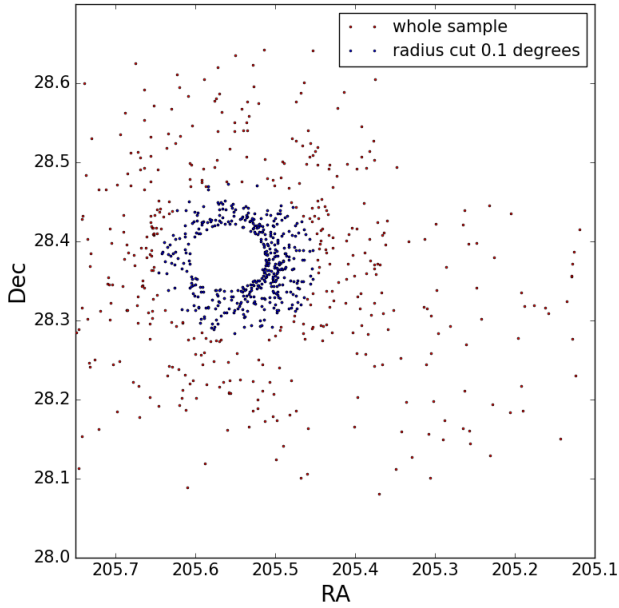


**Figure 11.** Figure showing RA and Dec positions (in degrees) of sources in INT image of M3 when considering the whole sample and when considering a radius of 0.1 degrees for the cluster.

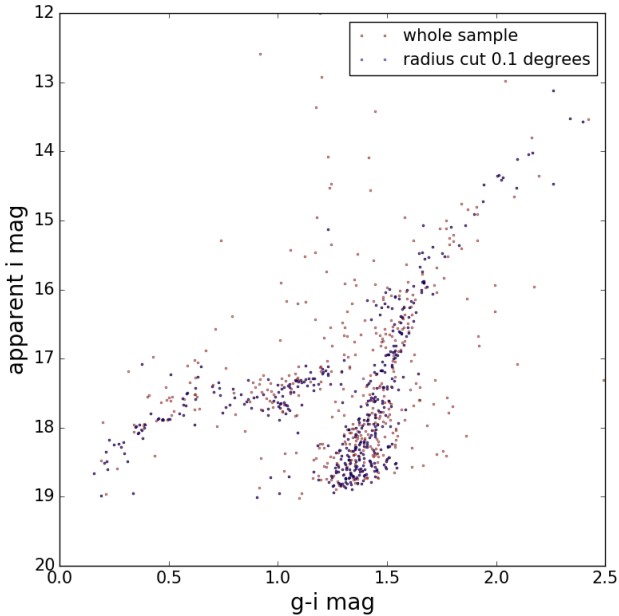


**Figure 12.** Figure showing how cutting the sample down to a radius of only 0.1 degree for M3 INT data changes the colour magnitude diagram.

excess based on values found from previous results (shown in table 3) and built upon methods outlined by Littlefair (2018).

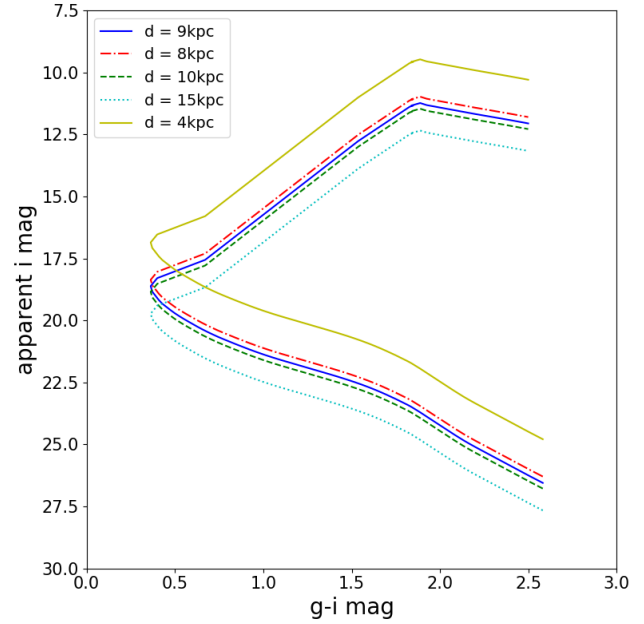


**Figure 13.** Figure demonstrating how distance changes the isochrone by displacing the model in the y direction.

#### 4.3.2 Determining Distances

In order to determine the distance to the clusters, the distance modulus equation 4 (where  $(m - M)$  is the distance modulus, and  $d$  is the distance in pc) is implemented into the model, allowing a value for distance to be entered and a corresponding value for the distance modulus is calculated.

$$m - M = 5 \log_{10} \left( \frac{d}{10} \right) \quad (4)$$

The HR diagrams are plotted using apparent magnitudes where as the isochrones are produced in absolute magnitudes, and so the vertical distance needed to translate the isochrone onto our data corresponds to the distance modulus. This means that the value input for distance, translates the isochrone such that it encompasses the data and this value corresponds to our distance estimate to the cluster under the assumption that all the stars in the cluster are at the same distance. Figure 13 shows how the isochrone shifts vertically to lower magnitudes with decreasing distance when all other parameters remain constant.

#### 4.3.3 Determining Age

Under the assumption that all the stars in the cluster form at the same time, then the most massive stars that are still in their hydrogen burning phase, on the main sequence, can be used to give an estimate for the clusters age. This is done by determining the location of the turn-off point, converting the colour index into a spectra type and using stellar lifetime to get a lower limit for the age of the cluster.

A model isochrone can be generated to show the current variations of the magnitudes of the population of stars with a certain age. Changing the age estimate will cause the shape

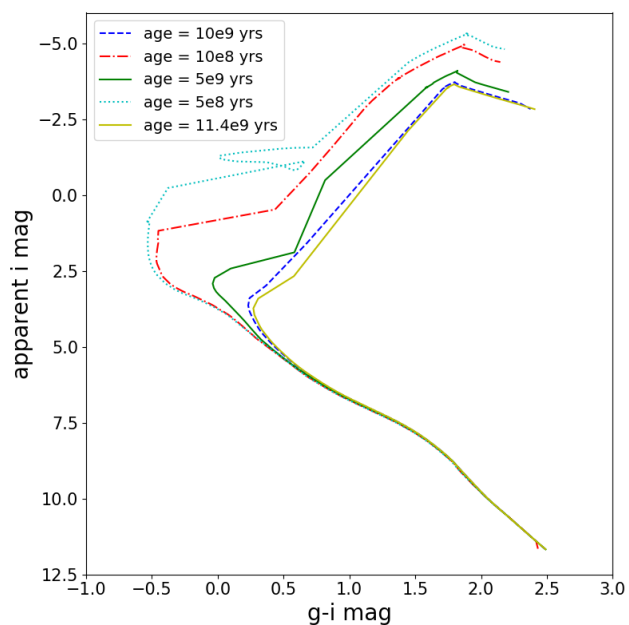


**Figure 14.** Figure demonstrating how the isochrone changes with age of the stellar population by the position of the turn-off point of the main sequence.

of the isochrone to change and cause the position of the turn-off point to change as illustrated in Figure 14. Therefore by matching the turn-off point of the data to the isochrone an estimate for the age of the cluster can be determined, as only the correct age of the isochrone will fit to the data. The lower limit on age using the Dartmouth isochrone is 2Myr (see Dotter et al. 2008).

#### 4.3.4 Metallicity

As shown in Figure 15 an increase in metallicity causes the isochrone to shift towards positive  $g-i$  magnitudes as this corresponds to the stars appearing redder due to metals in the stars absorbing light in shorter bluer wavelengths more than longer redder wavelengths. The value of the metallicity inputted can be altered until the isochrone fits the data and this value is taken to be our  $[Fe/H]$  for the cluster. The Dartmouth Stellar Evolution Database spans a range of metallicity  $[Fe/H]$  from 2.5 to +0.5 (see Dotter et al. 2008) which may limit our results.

#### 4.3.5 Accounting for Interstellar Extinction

Interstellar extinction arises from light scattering off the dust in the interstellar medium that lies in the line of sight between the observer and the target. The light emitted by cosmic object is scattered and absorbed by the grains of dust, thereby reducing the photon's energy and thus increasing their wavelength, producing a reddening effect (Trumpler 1930).

In the studying of Milky Way clusters it should also be noted that the majority of the dust in the galaxy resides at low galactic latitudes, in the disk, so clusters with a

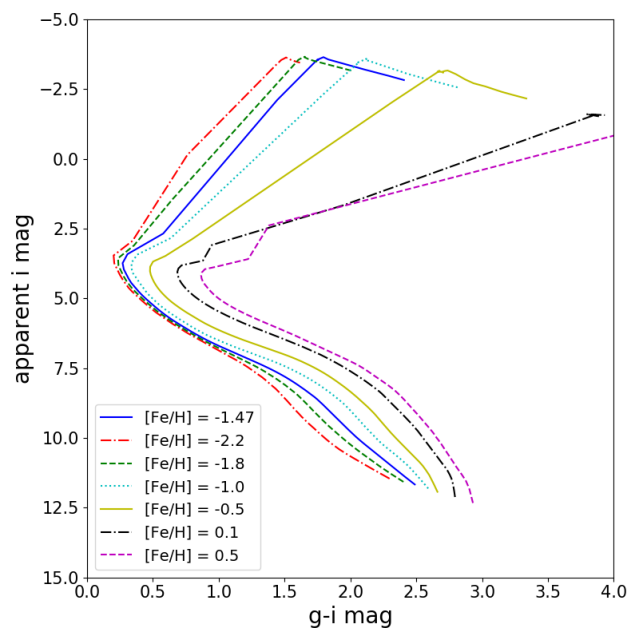


**Figure 15.** Figure demonstrating how different metallicity changes the isochrone by shifting the track in  $g-i$  magnitude and changing the structure of the track after the turn-off point.

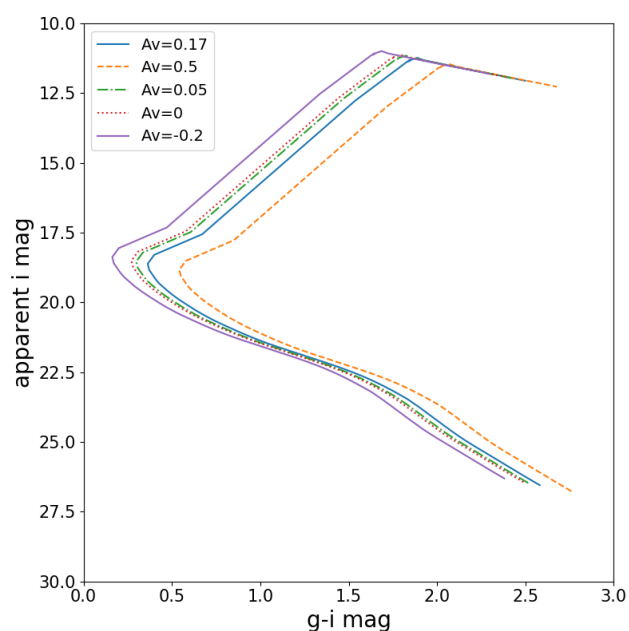


**Figure 16.** Figure demonstrating how the extinction in the  $v$  band ( $A_v$ ) changes the isochrone by a displacement in the  $x$  direction keeping the structure the same.

high galactic latitude have a negligible interstellar reddening (Gottlieb & Upson 1969).

Observed magnitudes are affected by interstellar extinction and so a correction is needed in order to compare observed data to theory. Isochrones are given in intrinsic magnitudes and in order to compare with our HR diagrams the

Cluster	Age (yrs)	Distance (kpc)	[Fe/H]	E(B-V)
M16	$\leq 10 \times 10^6$ <sup>(3)</sup>	2	-0.5	0.5
M67	$3.5 \times 10^9$	0.675	0.05	0.2
M3 <sup>1</sup>	$9.5 \times 10^9$	13	-2.5	0
M3 <sup>2</sup>	$11 \times 10^9$	5	-0.5	0
M71	$11 \times 10^9$	3	-0.8	0.25

**Table 6.** Table of our best fit values for age, distance, [Fe/H] and E(B-V) for each cluster studied. [1]: Hubble, [2]: INT, [3]: Age limitation found from that there is no turn-off. Typical uncertainties in these values are expected to be of the order of, in log scale,  $\pm 0.1$ dex, further work is needed to be able to quantify this further.

isochrone is converted to observed magnitudes using the extinction in the specific filter shown in Equation 5, where  $m_v$  is observed magnitude and  $m_{o,v}$  is the intrinsic magnitude.

$$A_\lambda = m_\lambda - m_{o,\lambda} \quad (5)$$

$A_\lambda$  is the magnitude in the filter centred on  $\lambda$  by which the object is observed to dim by. The colour excess, E(B-V) is a measure of the dust along the line of sight and is the measure this study will use to assess the interstellar extinction of the clusters studied. An extinction curve, which is a function of colour excess and provides a measure of the dust as a function of wavelength, by Calzetti<sup>1</sup> (Calzetti et al. 2000) was used in order to get the extinction in a specific filter with a central wavelength  $\lambda_{central}$ . Equation 6 takes the central wavelength of the filter and an E(B-V) estimate to convert into an extinction in that wavelength.

$$k(\lambda) = \frac{A(\lambda)}{E(B-V)} = a + \frac{b}{\lambda} + \frac{c}{\lambda^2} + \frac{d}{\lambda^3} \quad (6)$$

where a,b,c,d are constants in a given wavelength  $\lambda$ , and  $\lambda$  is the central wavelength of the filter used in the image.

By fitting isochrones to the data, an estimate for E(B-V) can be produced which can then use Equation 6 to correct for interstellar extinction.

## 5 RESULTS

In accordance with the methodology laid out in Section 4.1.2, the zero-points were first obtained for all the images used in this study, and are shown in Table 7. Using these and the catalogues produced from the reduced images, colour-magnitudes diagrams could be plotted, as described in Section 4.2 and isochrones fitted to these as described in Section 4.3.1. From these, the numerical results of this work were obtained using the methodology explained in Section 4, and are shown in Table 6.

### 5.1 Messier 16

Figure 17 shows the HR diagram plotted for the M16 results. It is a typical HRD for what is expected of this type of

<sup>1</sup> This extinction curve was originally generated to be used for star-burst galaxies but can be used for stellar populations and so is appropriate for this study.

Image	Catalogue	Matches	ZP
M16			
g	(Guarcello et al. 2010)	243	27.2924
i		692	26.62635
M67			
g	(Sandquist 2004)	463	27.8590002
i		492	26.972900
M3			
g	(Hartman et al. 2005)	17	26.725349
i		17	25.8708
F814W		17	23.27455
F555W		17	24.1186
M71			
g	(Geffert & Maintz 2000)	525	27.880001
i	(Roeser et al. 2010)	1824	26.49255

**Table 7.** Zero points calculated for each of the images used in this work, with catalogue and number of matches found to acquire the ZP also shown

cluster, as open clusters are young in comparison to globular clusters, so not many stars have started to turn off the main sequence yet.

There was quite a bit of noise with this image, which has been picked up by **SExtractor**, shown as the data points diffusing up toward the right in Figure 17, which could be caused by extinction (see Section 4.3.5) and/or field stars. These field stars are not associated with the cluster causing a spread of data points because of the varying apparent magnitudes as a result of the different distances to M16 and the particular composition of the individual stars surrounding the cluster. Specific to the cluster, extinction due to reddening varies drastically at a local level because of the Eagle Nebula that surrounds the stars. The stellar densities of the different regions creates fluctuations in the density of gas around M16. The spread of main sequence seen in Figure 17 can be explained by the dust variation in the different regions in the cluster, extinction shifts the data to redder colours and so stars from dusty regions are reddened more than stars from non dusty regions, hence the wide spread main sequence due to this localised extinction effect.

Martayan et al. (2008) finds the difference of reddening to be  $0.684 \leq E(B-V) \leq 1.866$  across the nebula. Selim et al. (2016) find a reddening of  $0.54 \pm 0.04$ . From the isochrone of best fit, shown in Figure 17, a reddening (E(B-V)) of 0.5 is found by this study. Isochrones cannot be used to determine the age of this cluster due to the lower limit restriction on the age of the Dartmouth University isochrone models, see Section 4.3.3 for more detail. However, since there are no red giants featured on the HR diagram for M16 (Figure 17) it is known that the cluster cannot be older than  $\leq 10$ Myr, as this is the time needed for these stars to form, as the shortest lifetime main sequence stars leave the hydrogen burning phase (Cannon 1970). Prior studies shown in Table 3, Section 2.1 demonstrate that the cluster is  $\leq 3.6$ Myr, as discussed in Section 2.1.1.

Isochrones are still able to estimate the other parameters, by setting the age to be the minimum value of  $2.5 \times 10^8$  yrs, and plotting an isochrone using estimates for the other parameters from Table 3 to see how this matches our data. From the isochrone, a distance to the cluster was found to be 2kpc which agrees with Selim et al. (2016) which in it-

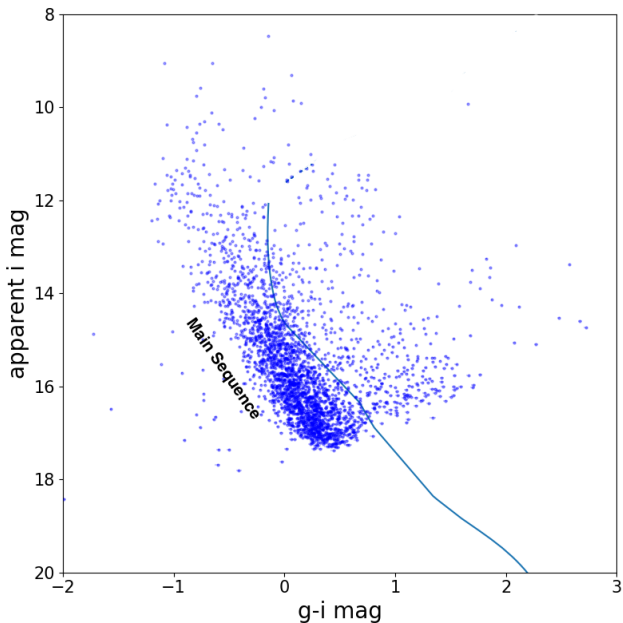


**Figure 17.** Colour-Magnitude plot for M16 in the g and i filters, with Dartmouth Isochrone overlaid with a distance of 2kpc,  $E(B-V)=0.5$  and  $[Fe/H]=-0.5$ . Age is determined by the fact that there are no red giants at  $\leq 10$ Myr.

self complies with the photometry from 2MASS from their study. Finally  $[Fe/H]$  of  $-0.50$  was found from plotting the isochrone which corresponds to 30% solar metallicity. This differs from a recent study which finds  $[Fe/H]$  of  $0.019$ , but as the only previous result of  $[Fe/H]$  contained in Table 3, this study's value is difficult to assess without further past results by which to compare with.

## 5.2 Messier 67

The HR diagram produced for M67 (see Figure 18) shows a distinctive main sequence, that is more heavily populated towards the bluer end of the spectrum with a clear turn off point from the main sequence at around  $m_i \approx 12$ , and with a horizontal branch and red giant branch.

It was therefore straight forward to obtain a value for the age of M67 from using results of past studies in Table 3, Section 2 and comparing the shape of the turn-off point to Figure 18 to adjust the parameters put into the isochrone model, as required. By changing the initial values in small increments a clear fit was produced with values; distance of 675pc, age of 3.5Gyr,  $E(B-V)=0.2$  and  $[Fe/H]=0.05$ . Two of these values do differ slightly from the previous results in Table 3. The distance is approximately  $100 \sim 150$ pc less than values found in other studies (see Table 3) which could be due to noise, from the image which has not been reduced fully, or error in the data taken from the catalogue. This noise could also be due to field stars in the image which **SExtractor** has wrongly identified as member stars of the cluster and have been included in the catalogues produced. The filters also have an effect on the noise. When matching catalogues for finding the ZP, corresponding filters between two catalogues overlap in the wavelength bands. However,

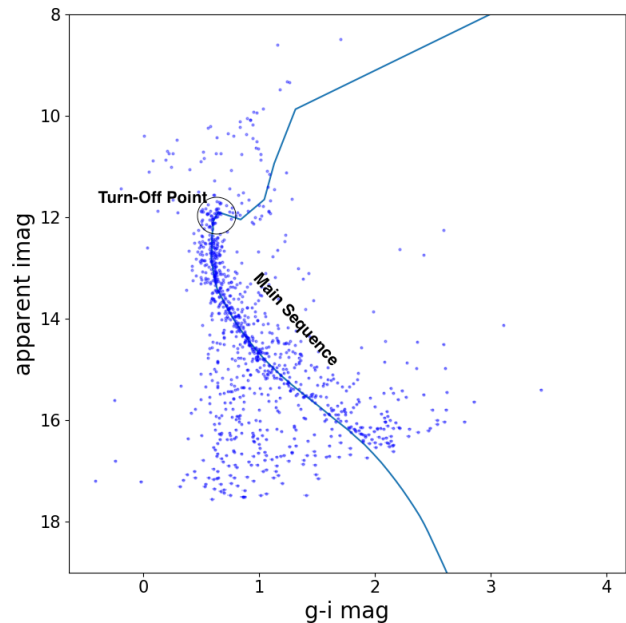


**Figure 18.** Dartmouth Isochrone plotted over M67 HR diagram (shown in Figure 9, Section 4.2), with parameters: distance 675pc, age  $3.5 \times 10^9$  yrs, metallicity of  $[Fe/H]=0.05$  and an extinction of  $E(B-V)=0.2$ .

if this overlap in bands is too small then the ZP will be adversely effected and this will result in increasing the apparent noise in the final HR diagram.

This value is of the same order of magnitude and so is a reasonable estimate, but further work could be undertaken by looking at more data in other filters to try and narrow down the possible sources of error. The extinction value ( $E(B-V)=0.2$ ) produced also differed, by one order of magnitude, compared to previous results (see Table 3) which estimated  $E(B-V)=0.046 \sim 0.004$ . The best fit metallicity value,  $[Fe/H]=0.05$ , agrees with previous studies. To further test this cluster, more images in different filters could be used to see whether the error in colour excess still arises.

## 5.3 Messier 3

M3 was the only cluster that used INT and Hubble data, with the Hubble data probing the inner regions of the cluster and the INT data containing only the out skirts of M3. The zero points for both the Hubble and INT images used for this cluster were found with only 17 matches to catalogue as shown in Table 7.

From the Hubble images, of the inner regions of M3, in F814W and F555W, a catalogue of 1763 stars was obtained which was then used to construct a colour magnitude diagram using F555W-F814W as the colour index. Using the isochrones outlined in Section 4.3, a best fit to this data was made to obtain an estimate for the clusters age, distance, metallicity and extinction. It proved difficult to fit an isochrone to this catalogue, mainly due to the extinction. For a best fit with values for age, distance and metallicity agreeing with theory (see Table 3) a negative  $E(B-V)$  value would be needed which is not possible, and so the  $E(B-V)$

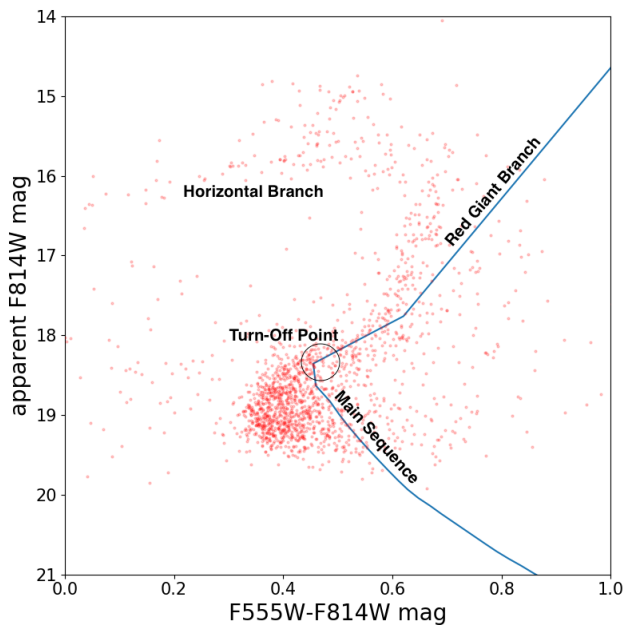


**Figure 19.** Colour-Magnitude plot for our catalogue of M3 from Hubble images that probe the inner regions of the cluster in the F555W and F814W filters. An isochrone generated using the Dartmouth Isochrones model is overlaid in blue which found the data with an age of  $9.5 \times 10^9$  yrs, distance of 13000pc,  $[\text{Fe}/\text{H}] = -2.5$  and  $E(B-V) = 0$ .

value was set to the smallest it can be ( $E(B-V) = 0$ ) and the other parameters were adjusted to get the best fit. This means that the extinction of this cluster could not be found from the data, but it could be predicted that this extinction is small. This agrees with theory (see Table 6) as M3 is a nearby cluster with low reddening so all studies researched found a low value for the  $E(B-V)$ . [Chieffi & Straniero \(1989\)](#) find a best fit using isochrones and use an  $E(B-V) = 0$ , so are in agreement with our results. The best fit distance to the cluster is found to be 13000pc which is in agreement with the order of magnitude of this estimate (see Table 3) and lies within the limits set out by past results.

An age of  $9.5 \times 10^9$  yrs is found for the cluster which lies within the limits set out by past results, this value is lower than more recent estimates of the clusters age but larger than the original estimate made by [Haselgrove & Hoyle \(1956\)](#). The best fit value for metallicity,  $[\text{Fe}/\text{H}]$ , is  $-2.5$  which is from the lower limit of the model used, rendering the value unreliable. It is roughly a factor of one lower than theory suggests for this cluster, see Table 3, and it is not clear whether this is due to the sample being of only the inner regions or possibly due to the issues with the extinction. Making the cluster more metal poor shifts the isochrone more blue-ward and so since the isochrone could not be shifted that way with extinction as a negative extinction is not possible, the metallicity was decreased instead. This factor of one discrepancy in the metallicity corresponds to a factor of ten times the solar metallicity and so it is a large disagreement to theory.

For the INT image, a catalogue of 834 stars was obtained across the entire image, and from this produced a

colour magnitude diagram using  $g-i$  as the colour index. Fitting an isochrone to this sample also proved difficult, as it appears that the sample contains no, or very little, main sequence stars, instead only stars that have already turned off of the main sequence. The  $i$  filter is similar to the F814W filter used for the Hubble image and the main sequence turn off point seems to correspond to an F814W magnitude of approximately 18, however our colour magnitude diagram for the INT catalogue begins at lower ( $i$ ) magnitudes of around 16, suggesting that this sample does not contain any main sequence stars. This shift in data could be a consequence of the different filters having a larger effect than expected on  $i$  magnitude values. It could also suggest that the stars in the INT catalogue are actually field stars that do not belong to the cluster and that is why this is not seen on the main sequence. However, since there is clear structures in this diagram, assumptions can be made so that this is not the case and that the sample does in fact only contains stars that have already turned off the main sequence. This proves difficult when fitting an isochrone as it fits best by the main sequence and turn off point, instead to fit the isochrones to the other structures seen, past the turn off point, mainly the RGB (red giant branch). Similar to what is seen with the Hubble catalogue and also in past results, the extinction of this cluster is very low requiring the use an extinction,  $E(B-V) = 0$  in order to make our fit. The distance found is lower than that found with the Hubble data, 5000pc. This distance estimate still lies within the limits set by theory, see Table 3 and is in good agreement with the most recent estimate by [Watkins & van der Marel \(2017\)](#). The isochrone has an age of  $11 \times 10^9$  yrs which agrees almost perfectly with the most recent result by [Thassana & Maithong \(2017\)](#). The metallicity obtained from the INT data is very different to that with the Hubble data. The results find an  $[\text{Fe}/\text{H}] = -0.5$  which is, as with the Hubble estimate, roughly a factor of 1 away from what theory predicts, however in the opposite direction to previously found with Hubble.

This is an issue as neither our INT results, Hubble results or past results agree upon a value for the metallicity of the cluster. The INT data only contains stars from the outer regions of the cluster and also only post main sequence stars, whereas the Hubble data probes the inner regions of the cluster and contains stars along the main sequence. This could explain our differences in the values obtained. The results may suggest that the cluster has a lower metallicity in the inner regions but further work is needed in order to investigate this claim further. Our results also suggest that the inner regions are younger than the outer regions of the cluster, thus suggesting the cluster formed inside out. Again, further work is needed to investigate this claim further. In both colour magnitude diagrams for M3, Figures 19 and 20, the majority of the structures expected to be seen are present, as labelled. The diagrams also suggest a population of blue stragglers in the cluster, supporting theory that these stars are present in M3 ([Bailyn & Pinsonneault 1995](#)).

#### 5.4 Messier 71

There are two clearly defined regions in the HRD for M71 (see Figure 21) reasoned to be possibly due to the different exposure times of the  $g$  and  $i$  filter images for M71 than for

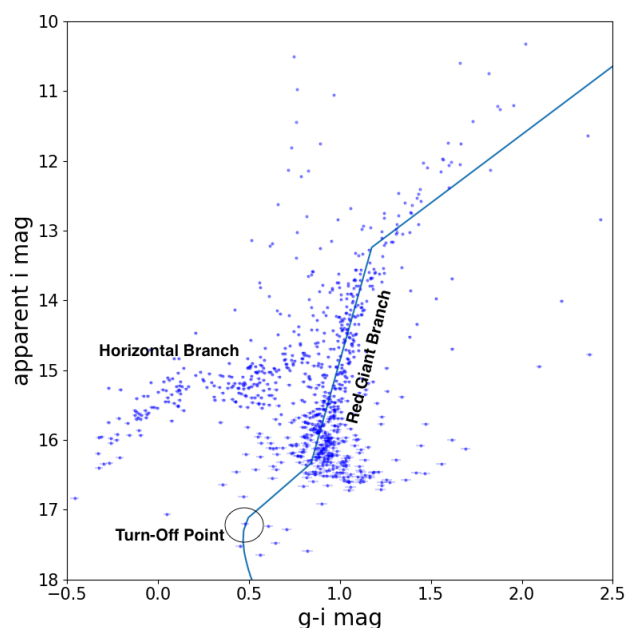


**Figure 20.** Colour-Magnitude plot of M3 from the INT data in the g and i filters. An isochrone generated using the Dartmouth Isochrones model is overlaid in blue which best fits this data with an age of  $11 \times 10^9$  yrs, distance to the cluster of 5000pc,  $[\text{Fe}/\text{H}] = -0.5$  and  $E(\text{B}-\text{V}) = 0$ .

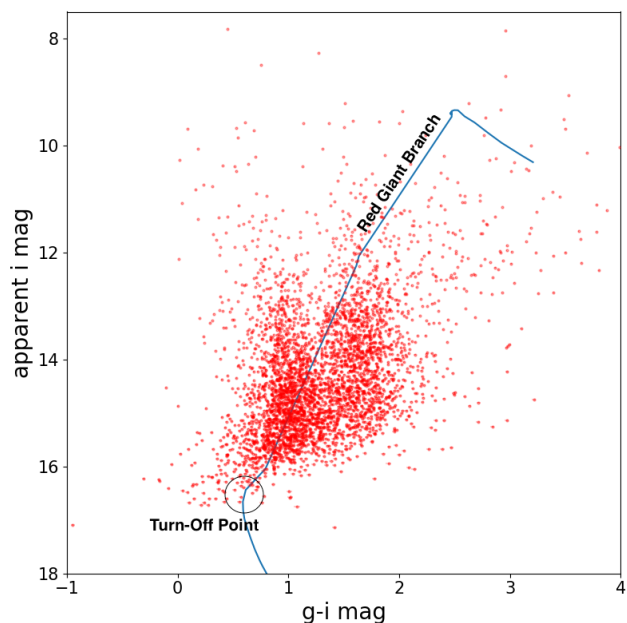


**Figure 21.** Colour magnitude diagram for M71 using INT data in the g and i filter. An isochrone from Dartmouth library is overlaid in blue with a distance value of 3000pc, age of  $11 \times 10^9$  yrs,  $[\text{Fe}/\text{H}] = -0.8$  and  $E(\text{B}-\text{V}) = 0.25$ .

the other clusters (see Table 4, Section 2.3), possibly resulting in this strange effect of two distinct populations of stars relating to the two filter bands used. Therefore it was not possible to produce a clear fit of the isochrone to the data but a best fit approach was used where the isochrone was fitted towards the centre of the data. The resulting isochrone was fitting by inputting a distance of 3000pc, age of  $11 \times 10^9$  yrs,  $[\text{Fe}/\text{H}] = -0.8$  and  $E(\text{B}-\text{V}) = 0.25$ . The colour-magnitude diagram with this isochrone is shown in Figure 21.

By comparing these results to those found in previous studies (see Table 3, Section 2) the  $E(\text{B}-\text{V})$  and  $[\text{Fe}/\text{H}]$  found by this work are in agreement with past results;  $E(\text{B}-\text{V})$  to within  $\pm 0.07$  and agrees perfectly with many studies (e.g. Cohen et al. 2001; Oliveira et al. 2013; An 2008; Harris 1996) and  $[\text{Fe}/\text{H}]$  to within  $\sim \pm 0.4$  and agrees with Salaris & Cassisi (1997). The distance result of 3000pc is of the same order of magnitude as past results, which are on average, approximately 4.5kpc. However, this work’s distance result is still 800pc less than the smallest distance obtained by a previous study (Salaris & Cassisi 1997) displayed in Table 3. This study’s age estimation is in agreement with some previous results (see J. Davidge & A. Simons 1994; Cecco et al. 2014) and is of the same order as all other’s displayed in Table 3 bar one (Arp & Hartwick 1971), which is significantly lower than any other result and is also the oldest study included in Table 3.

## 6 DISCUSSION

### 6.1 Open Clusters

As mentioned previously in Sections 2.1.1 & 2.1.2, M16 is a very youthful open cluster, with an age of the order of Myrs (see Table 3), while M67 is more on the order of a globular cluster, with an age of the order of Gyrs (also see Table 3). Therefore it is not surprising that there is such stark differences between the isochrone fitted data for M16 (see Figure 17) and M67 (see Figure 18). M16 is dominated by main sequence stars, with no visible turn-off point, though this is not surprising given it is only a few million years old so very few stars would have progressed beyond the main sequence. However, M67 has a distinctive main sequence and a clear turn-off point, red giant and horizontal branches, which are not present in M16. This is not unexpected given the age of M67, similar to globular clusters, the bluer evolutionary structures on the HR diagram have had time to mature.

It should, however, be kept in mind that M67 may be similar to globular clusters in the structures that are seen in Figure 18, but it is still distinctive from a globular cluster as can be seen in this study’s data. Being an open cluster, M67 is less dense and is irregularly shaped compared to an ordered, dense globular cluster (see Section 1) which gives rise to issues in imaging the globular clusters clearly. This can be seen in the problems faced in obtaining clear results and plots for the globular clusters (see Sections 5.3 & 5.4). These same issues are not seen for M67, as obtaining a HR diagram with clear structure was possible.

As discussed in Section 5.1, the HR diagram shows less structure, and a very broad main sequence possibly due to differing levels of extinction for stars due to the different structures of dust present in M16. These give rise to structures such as the famous ‘Pillars of creation’ in M16, while

M67 has few distinguishing features of dust which therefore negates this differing, localised dust extinction seen in M16.

## 6.2 Globular Clusters

There is a sharp main sequence turn off in our colour magnitude diagrams for M3, see Figure 19, which is typical of a globular cluster, suggesting that the stars within the cluster all formed at the same time. The main sequence is also very narrow, suggesting stars in the cluster have similar chemical makeup. The main sequence turn off point is not seen in our colour magnitude diagram for M3 using the INT data, see Figure 20, since our data appears to only contain stars that have already left the main sequence. It is still clear to see a narrow red giant and horizontal branch as expected. There is no clear main sequence turn off for the INT data of M71, see Figure 21, as the isochrone fit suggests that all the stars are post main sequence. Both the M3 and M71 INT data only contains stars in the outer regions of the cluster as the central regions needed to be masked (see Section 5.3 & 5.4) and both samples appear to contain no main sequence stars. This could suggest that the stars in the cluster that are still on the main sequence reside in the central bulge. However, this could be a result of issues with our data.

Clusters of higher metallicity have been observed to have giant branches that are shallower, fainter and redder (Sandage & Wallerstein 1960). M71 is a higher metallicity cluster than M3, according to past results (see Table 3) and this work's (see Table 6) but a clear red giant branch for M71 is not seen in the colour magnitude diagram (Figure 21) and so this conclusion cannot be drawn from the two globular clusters that have been studied here.

Red giant and horizontal branches can be identified in our data for M3 (see Figures 19 & 20) but as the data for M71 is not as clear (see Figure 21) these branches are not distinct, therefore these stars cannot be identified.

## 7 CONCLUSIONS

This study has investigated two open clusters and two globular clusters. The 'GOC' data reduction pipeline was developed and presented, a reduction pipeline that is capable of taking raw FITS files from the INT to produce useable data, that could now be tasked with reducing other images from the INT.

Using **SExtractor**, the zero points of each image were found, then a catalogue of the stars were produced. Catalogues between two filters (g and i for the INT images, F555W and F814W for the Hubble images) were matched and used to produce a colour-magnitude diagram for each of the clusters studied. Using an isochrone fitting package downloaded from Dartmouth University and a **Python** script for interstellar extinction, isochrones were fitted over the HR diagrams for each cluster. Incremental adjustments were made to original values of distance, age, metallicity and extinction found from past results to best fit the isochrones onto the observed data, and to determine estimates for these for the clusters investigated.

For the open clusters the data for M16 and M67 produced the following results: M16 is the youngest cluster studied and this is confirmed by our results constraining the age.

Due to the limiting isochrone models available a more accurate age could not be determined. In M16 even the most massive, hottest stars seem to be on the main sequence, implying an age of  $\leq 10$  Myrs. Our models predict M16 to be at a distance of 2kpc with a  $[\text{Fe}/\text{H}] = -0.5$ , and the highest of our calculated reddening,  $E(\text{B}-\text{V}) = 0.5$ . M67 is one of the oldest open clusters, which agrees with the isochrone that predicts an age of  $3.5 \times 10^9$  years. M67 is found to be closer, with a distance of 0.675kpc. This cluster is more metal rich than the younger, M16, which can be seen in our results with a  $[\text{Fe}/\text{H}] = 0.05$ . M67 is not associated with dust and nebulae like M16 is, and this explains the lower  $E(\text{B}-\text{V}) = 0.2$  for M67.

For the globular clusters M3 and M71, the following results were: M3 *HST* data of the inner regions of the cluster gave an age estimate of  $9.5 \times 10^9$  years, a distance of 13kpc,  $[\text{Fe}/\text{H}] = -2.5$ , and  $E(\text{B}-\text{V}) = 0$ . The M3 INT data gave an older age estimate of  $11 \times 10^9$  years. The INT data contains only stars from the outer regions of the cluster and the Hubble only inner regions and so the differing in parameters such as age could suggest that the different regions formed at different times. The INT gives a distance estimate of 5kpc,  $[\text{Fe}/\text{H}] = -0.5$ , and  $E(\text{B}-\text{V}) = 0$ . M3 is a high galactic latitude cluster and as such is not expected to have a high  $E(\text{B}-\text{V})$  value. M71 is found to have an age of  $11 \times 10^9$  years similar to the age seen for M3. With a distance of 3kpc,  $[\text{Fe}/\text{H}] = -0.8$ , and  $E(\text{B}-\text{V}) = 0.25$ .

Obvious comparisons between the open and globular clusters, that this work has shown, often lie in the difference between metallicity, in line with what past results have shown in Table 3. Although the differences are small, the globular clusters are generally more metal-poor than the open clusters. This can be interpreted as a consequence of the cosmic time and environment in which the different stellar clusters formed. Globular clusters formed before the Universe was metal rich, as previously mentioned. Other differences lie in ages, which is the case with M16 being far younger than M3 and M71, which this study has shown. However M67 is of the same order of magnitude as the globular clusters' age. Therefore M67 is interesting in this sense, and a useful example of the key differences between open and globular clusters that can be shown by the findings of this investigation. Although M67 has an age of the order to that of a globular cluster, it is clear from its structure on the HR diagram that it is an open cluster. This is because the cluster has a lower stellar density at its core, making it easier to resolve, as was found by this work, and therefore greater clarity on the HR diagram produced by this research.

The issues faced by this investigation in attempting to resolve the dense core regions of globular clusters have reinforced the same issues that have plagued previous studies into these clusters. Attempted solutions to these issues have been discussed and attempts to implement them explored.

The other major issue faced this study that have been discussed, surrounds determining the age of young open clusters. Potential solutions to this could be to find new models that accommodate for much younger clusters and allow better estimations of values for M16 to be made.

Future work could involve studying a larger sample of open and globular clusters, in order to highlight the differences between the two types of clusters and also differences within each cluster category. Incorporating more Hub-

ble data will improve our estimates for the different clusters due to the images being of higher quality and also able to resolve regions of globular clusters the INT is unable to. The different metallicities between the two types of clusters, implying the different environments in which clusters form, can be studied to investigate how these clusters formed and constrain the types of gas clouds these clusters form from, via observation and also simulations (Li et al. 2017). The evolution of the Galaxy can be further understood by studying Milky Way open and globular clusters (Reddy et al. 2016). Since open clusters still form within the spiral arms of the Milky Way, the understanding of this process is well studied when compared with the formation of globular cluster systems, which are no longer forming in the Milky Way. Further investigations to develop this understanding of globular clusters could be to study the stellar clusters seen at extremely high redshift, theorised to be globular cluster progenitors, these young massive clusters can provide us with a history of clusters over time and improve our understanding of how these systems formed (e.g. Walker et al. 2015, 2016). Thus, relating these high redshift observations of young massive clusters to globular clusters within the Milky Way can further our understanding of the formation of globular clusters within the Galaxy, which is vital to be able to understand the formation of the Galaxy itself.

## ACKNOWLEDGEMENTS

The authors are thankful to Dr David Sobral, who has assisted us in producing this work, and providing code for the GOC Pipeline (see Sobral et al. 2016). We are also grateful to Dartmouth University and their isochrone fitting package (Dotter et al. 2008). Based on observations made with the INT operated on the island of La Palma by the Isaac Newton Group of Telescopes in the Spanish Observatorio del Roque de los Muchachos of the Instituto de Astrofísica de Canarias Programme N1. Based on observations made with the NASA/ESA Hubble Space Telescope, obtained from the data archive at the Space Telescope Science Institute. STScI is operated by the Association of Universities for Research in Astronomy, Inc. under NASA contract NAS 5-26555, Proposal 6805. This study has benefited immensely from the publicly available programming language Python, including NumPy & SciPy (Van Der Walt et al. 2011; Jones et al. 2001), Matplotlib (Hunter 2007), Astropy (Astropy Collaboration et al. 2013). There has also been great benefit from the publicly available programs; catalogue producer SExtractor (Bertin & Arnouts 1996), the astrometric correction programs SCAMP and SWARP (Bertin 2006, 2010) and the TOPCAT analysis program (Taylor 2005). This research has made use of the VizieR catalogue access tool, CDS, Strasbourg, France (Ochsenbein, F. et al. 2000).

## REFERENCES

An D., 2008, PhD thesis, The Ohio State University  
 Arp H. C., Hartwick F. D. A., 1971, *ApJ*, **167**, 499  
 Astropy Collaboration et al., 2013, *A&A*, **558**, A33  
 Baily C. D., Pinsonneault M. H., 1995, *ApJ*, **439**, 705  
 Baumgardt H., De Marchi G., Kroupa P., 2008, *ApJ*, **685**, 247

Bertin E., 2006, in Gabriel C., Arviset C., Ponz D., Enrique S., eds, *Astronomical Society of the Pacific Conference Series Vol. 351, Astronomical Data Analysis Software and Systems XV*. p. 112  
 Bertin E., 2010, SWarp: Resampling and Co-adding FITS Images Together, *Astrophysics Source Code Library* (ascl:1010.068)  
 Bertin E., Arnouts S., 1996, *A&AS*, **117**, 393  
 Boesgaard A. M., Steigman G., 1985, *ARA&A*, **23**, 319  
 Bohm-Vitense E., 1981, *ARA&A*, **19**, 295  
 Bolte M., 1989, *ApJ*, **341**, 168  
 Bonatto C., Santos Jr. J. F. C., Bica E., 2006, *A&A*, **445**, 567  
 Bonnell I. A., Davies M. B., 1998, *MNRAS*, **295**, 691  
 Boyle W. S., Smith G. E., 2013, Charge Coupled Semiconductor Devices, <https://onlinelibrary.wiley.com/doi/abs/10.1002/j.1538-7305.1970.tb01790.x>  
 Calzetti D., Armus L., Bohlin R. C., Kinney A. L., Koornneef J., Storchi-Bergmann T., 2000, *ApJ*, **533**, 682  
 Cannon R., 1970, *MNRAS*, **150**, 111  
 Carretta E., Gratton R. G., 1997, *A&AS*, **121**, 95  
 Cecco A. D., et al., 2014, On the absolute age of the globular cluster M71, **85**  
 Cecco A. D., et al., 2015, *AJ*, **150**, 51  
 Charlot S., Bruzual A. G., 1991, *ApJ*, **367**, 126  
 Chieffi A., Straniero O., 1989, *ApJS*, **71**, 47  
 Chiosi C., Nasi E., 1974, *A&A*, **35**, 81  
 Cohen J. G., Behr B. B., Briley M. M., 2001, *AJ*, **122**, 1420  
 Cudworth K., 1979, *AJ*, **84**, 1312  
 Dias W., Alessi B., Moitinho A., Lépine J., 2002, *A&A*, **389**, 871  
 Dotter A., Chaboyer B., Jevremović D., Kostov V., Baron E., Ferguson J. W., 2008, *ApJS*, **178**, 89  
 Dressel L., 2008, *Wide Field and Planetary Camera 2 Instrument Handbook*  
 Ferraro F. R., Paltrinieri B., Pecci F. F., Cacciari C., Dorman B., Rood R. T., 1997, *The Astrophysical Journal Letters*, **484**, L145  
 Ferraro F., Messineo M., Pecci F. F., De Palo M., Straniero O., Chieffi A., Limongi M., 1999, *AJ*, **118**, 1738  
 Ferraro F. R., Sills A., Rood R. T., Paltrinieri B., Buonanno R., 2003, *ApJ*, **588**, 464  
 Friel E., 1995, *ARA&A*, **33**, 381  
 G. Cohen J., 1980, *ApJ*, **241**, 981  
 Gao L., Jenkins A., Frenk C. S., Helly J. C., Theuns T., Navarro J., White S. D. M., Springel V., 2010, *MNRAS*, **403**, 1283  
 Geffert M., Maintz G., 2000, *VizieR Online Data Catalog*, **414**  
 Goldsbury R., Richer H. B., Anderson J., Dotter A., Sarajedini A., Woodley K., 2010, *AJ*, **140**, 1830  
 Gottlieb D. M., Upson W. L., 1969, *ApJ*, **157**, 611  
 Gratton R., 1985, *A&A*, **147**, 169  
 Guarcello M. G., Micela G., Damiani F., Peres G., Prisinzano L., Sciortino S., 2009, *A&A*, **496**, 453  
 Guarcello M. G., Micela G., Peres G., Prisinzano L., Sciortino S., 2010, *A&A*, **521**, A61  
 Harris W. E., 1996, *AJ*, **112**, 1487  
 Harris W. E., Racine R., 1979, *ARA&A*, **17**, 241  
 Hartman J. D., Kaluzny J., Szentgyorgyi A., Stanek K. Z., 2005, *AJ*, **129**, 1596  
 Haselgrove C. B., Hoyle F., 1956, *MNRAS*, **116**, 527  
 Heasley J. N., Christian C. A., 1991, in Janes K., ed., *Astronomical Society of the Pacific Conference Series Vol. 13, The Formation and Evolution of Star Clusters*. p. 266  
 Heggie D., Hut P., 2003, *The Gravitational Million Body Problem: A Multidisciplinary Approach to Star Cluster Dynamics*. Cambridge University Press, [doi:10.1017/CBO9781139164535](https://doi.org/10.1017/CBO9781139164535)  
 Hillenbrand L. A., Massey P., Strom S. E., Merrill K. M., 1993, *AJ*, **106**, 1906  
 Hills J., Day C., 1976, *ApJ*, **17**, 87  
 Hodder P. J. C., Nemeč J. M., Richer H. B., Fahlman G. G., 1992, *AJ*, **103**, 460

- Hunter J. D., 2007, *Computing In Science & Engineering*, 9, 90
- ING 2018b, <http://www.ing.iac.es/astrometry/telescopes/int/>
- ING 2018a, ING Filter Database, <http://catserver.ing.iac.es/filter/list.php?instrument=WFC>
- 2018c, Site Quality, <http://www.ing.iac.es/Astronomy/observing/conditions/>
- Iben Jr I., 1974, *ARA&A*, 12, 215
- Ishiyama T., Sudo K., Yokoi S., Hasegawa K., Tominaga N., Susa H., 2016, *ApJ*, 826, 9
- J. Davidge T., A. Simons D., 1994, *ApJ*, 435, 207
- J. Tripicco M., Dorman B., A. Bell R., 1993, *AJ*, 106
- Janes K., Demarque P., 1983, *ApJ*, 264, 206
- Johnson J. L., 2015, *MNRAS*, 453, 2771
- Jones E., Oliphant T., Peterson P., et al., 2001, SciPy: Open source scientific tools for Python, <http://www.scipy.org/>
- Kai-ping T., Jun-liang Z., Rong-shi P., Yan-ping H., 1993, *Chinese Astronomy and Astrophysics*, 17, 195
- Kharchenko N. V., Piskunov A. E., Röser S., Schilbach E., Scholz R.-D., 2005a, *A&A*, 438, 1163
- Kharchenko N., Piskunov A., Röser S., Schilbach E., Scholz R.-D., 2005b, *A&A*, 438, 1163
- King I. R., Sosin C., Cool A. M., 1995, *ApJ*, 452
- Kraft R. P., Sneden C., Langer G., Prosser C. F., 1992, *AJ*, 104, 645
- Krauss L. M., Chaboyer B., 2003, *Science*, 299, 65
- Kuhn M. A., Getman K. V., Feigelson E. D., 2015, *ApJ*, 802, 60
- Leonard P. J., 1996, *ApJ*, 470, 521
- Li H., Gnedin O. Y., Gnedin N. Y., Meng X., Semenov V. A., Kravtsov A. V., 2017, *ApJ*, 834, 69
- Littlefair S., 2018, Using the Isochrones Library, [http://slittlefair.staff.shef.ac.uk/teaching/phy241/resources/plotting\\_isochrones.html](http://slittlefair.staff.shef.ac.uk/teaching/phy241/resources/plotting_isochrones.html)
- Livio M., 1993, in *Blue Stragglers*. p. 3
- Marconi M., Caputo F., Di Criscienzo M., Castellani M., 2003, *ApJ*, 596, 299
- Martayan C., Floquet M., Hubert A.-M., Neiner C., Fremat Y., Baade D., Fabregat J., 2008, *A&A*, 489, 459
- Meylan G., Heggie D., 1997, *The Astronomy and Astrophysics Review*, 8, 1
- Nightingale N. S., Buscher D. F., 1991, *MNRAS*, 251, 155
- Nishimura et al., 2017, arXiv.org
- Ochsenbein, F. Bauer, P. Marcout, J. 2000, *Astron. Astrophys. Suppl. Ser.*, 143, 23
- Oliveira A., Monteiro H., Dias W., Caetano T., 2013, *A&A*, 557
- Önehag A., Korn A., Gustafsson B., Stempels E., Vandenberg D. A., 2011, *Astronomy & Astrophysics*, 528
- Padmanabhan P., 2000, *Theoretical astrophysics. Vol. 1: Astrophysical processes. Vol. 1*, Cambridge University Press
- Paez E., Roger C. M., Straniero O., 1990, *Astrophysics and Space Science*, 169, 15
- Pichardo B., Moreno E., Allen C., Bedin L. R., Bellini A., Pasquini L., 2012, *AJ*, 143, 73
- Reddy A. B., Lambert D. L., Giridhar S., 2016, *MNRAS*, 463, 4366
- Roeser S., Demleitner M., Schilbach E., 2010, *AJ*, 139, 2440
- Salaris M., Cassisi S., 1997, *MNRAS*, 289, 406
- Salpeter E. E., 1955, *ApJ*, 121, 161
- Sandage A., Cacciari C., 1990, *ApJ*, 350, 645
- Sandage A., Wallerstein G., 1960, *ApJ*, 131, 598
- Sanders W. L., 1977, *A&AS*, 27, 89
- Sandquist E. L., 2004, *MNRAS*, 347, 101
- Sarajedini A., Dotter A., Kirkpatrick A., 2009, *ApJ*, 698, 1872
- Sarmiento R., Scannapieco E., Cohen S., 2018, *ApJ*, 854, 75
- Sato K., Audouze J., 2012, *Primordial Nucleosynthesis and Evolution of Early Universe*. Springer Science & Business Media, Schaefer D., 2002, *A&A*, 382, 28
- Schlaufman K. C., Thompson I. B., Casey A. R., 2018, *ApJ*, 867, 98
- Selim I., Essam A., HENDY Y., BENDARY R., 2016, *NRIAG Journal of Astronomy and Geophysics*, 5, 16
- Sobral D., Matthee J., Darvish B., Schaefer D., Mobasher B., Rottgering H. J. A., Santos S., Hemmati S., 2015, *ApJ*, 808, 139
- Sobral D., et al., 2016, *MNRAS*, 466, 1242
- Sorensen P., Azzaro M., MÃndez J., 2018, <http://catserver.ing.iac.es/staralt/index.php>
- Stryker L., 1993, *Publications of the Astronomical Society of the Pacific*, 105, 1081
- Taylor R. J. R. J., 1981, *The stars : their structure and evolution*. Wykeham science series ; 10, Taylor & Francis, London ; Philadelphia
- Taylor M. B., 2005, in Shopbell P., Britton M., Ebert R., eds, *Astronomical Society of the Pacific Conference Series Vol. 347, Astronomical Data Analysis Software and Systems XIV*. p. 29
- Taylor M., 2013, *Starlink User Note*, 253
- Taylor B. J., Joner M. D., 2005, *ApJS*, 159, 100
- Thassana C., Maithong W., 2017, *Jurnal Sains Dasar*, 6, 98
- Trenti M., Shull J. M., 2010, *ApJ*, 712, 435
- Trumpler R. J., 1930, *Lick Observatory Bulletin*, 14, 154
- Umemura M., Susa H., 2001, in *The Physics of Galaxy Formation*.
- Van Der Walt S., Colbert S. C., Varoquaux G., 2011, *Computing in Science & Engineering*, 13, 22
- VandenBerg D. A., Bergbusch P. A., Ferguson J. W., Edvardsson B., 2014, *ApJ*, 794, 72
- Vanderbeke J., et al., 2013, *MNRAS*, 437, 1725
- Walker D., Longmore S., Bastian N., Kruijssen J., Rathborne J., Jackson J., Foster J., Contreras Y., 2015, *MNRAS*, 449, 715
- Walker D., Longmore S., Bastian N., Kruijssen J., Rathborne J., Galván-Madrid R., Liu H., 2016, *MNRAS*, 457, 4536
- Watkins L. L., Van der Marel R. P., 2017, *ApJ*, 839, 89
- Watkins L. L., van der Marel R. P., 2017, *ApJ*, 839, 89
- Weiss A., Abel T. G., Hill V., 2000, *First Stars*. Springer-Verlag
- Wu Z.-Y., Zhou X., Ma J., Du C.-H., 2009, *MNRAS*, 399, 2146
- Yim H.-S., Chun M.-S., Byun Y.-I., Sohn Y.-J., 2004, *Journal of Astronomy and Space Sciences*, 21, 1
- Zapata P. M., 2016, *Characterisation of the open cluster M67*
- Zinn R., 1985, *ApJ*, 293, 424
- Zocchi A., 2014, PhD thesis, Universit'a degli Studi di Milano

## APPENDIX A: OVERVIEW OF GOC PIPELINE

### A1 Organisation of Pipeline

The image reduction (Stage 1) is the first step of our methodology and is handled by a Python script called `reduce.py`. It is located in the pipeline directory with all the numerous config files required at various steps and folders for each step of the reduction. These folders have to be created manually for each cluster and each filter one may want to reduce and must follow a set naming pattern for the script to find the correct files.

These names are defined by two user defined strings: cluster and filter. Using these as the only words in folders and image names that differs, `reduce.py` can find the files it requires but it does lead to a complex filing structure that could easily be constructed incorrectly if one would wish to reduce a different image.

The user can then select what step of the image reduction to perform, by entering the number corresponding to the option in a menu. This avoids having to run the entire program (which can be quite lengthy) to simply SWARP an

image for example, rather than the full process outlined in Section 3.1.

To be able to keep this organised, the files are arranged by cluster and filter into folders for each stage of the image reduction. The raw images start in `.\Raw\cluster_name\filter_band` with folders for the flats and biases as there can be about 10 of these. The split images are sent to a folder named `.\Unreduced\cluster_name\filter_band` and are prefixed with the CCD number. This is required as the script searches for files based on a naming pattern of CCD number, cluster name and filter band.

## A2 Correcting Headers

After the science images are reduced (as explained in Section 3.1), the reduced images are then sent to `.\Reduced\cluster_name\filter_band` and are named `\CCD_cluster_reduced_filter.fit`, with their headers passed over from the raw images split up earlier.

This stage of the reduction encountered many coding issues. Principally issues surrounding deprecated methods of `Astropy` being used by the code supplied to us from Dr Sobral (see Sobral et al. 2016), that contained the unique corrections to the headers which was written in `Python 2` not `Python 3` which `reduce.py` is written in. There is a small but important difference in syntax between these two versions of the language but can result in issues. The initial fixes for deprecated methods had unexpected results, whereby values of key word fields in the headers were subtracted from each pixel's count rather than removing the key word as intended. Commenting out these methods at this stage caused unexpected consequences later that are discussed in Appendix A4

When these issues were overcome by either commenting out deprecated methods or using appropriate current ones, the reduced images with fixed headers are then saved as `\CCD_cluster_reducedFixed_filter.fit`.

## A3 SCAMPing

`sexscamp.sex` is the config file which makes sure the catalogues are produced in the format `SCAMP` expects and configure how `SExtractor` runs over the image, such as sigma thresholds, size of apertures around sources it detects (stars). We opted to leave these parameters to default settings which will affect the calibration of our images and as such, the potential errors introduced into our results.

`sexscamp.scamp` is the config file for `SCAMP`. We encountered issues with an error being produced pertaining to `SCAMP` not locating any reference catalogues for our images:

```
No such reference catalogue for sky zone.
Wrong sky zone?
```

We initially believed this was due to the config file giving a server address (from which it loads reference catalogues from surveys such as SDSS or 2MASS) that was no longer in use as it was from 2012. However this was actually an issue with a missing API which queries the server for the requested catalogue which is defined in the config file. This error was difficult to track down due to the complexity of how

`SExtractor` and `SCAMP` works. They depend on the images one supplies them, the configuration files and a plethora of other software needed to run them. Many of these are Unix based which were unfamiliar to us.

With these issues fixed, the 'SCAMPed' images and catalogues produced by `SCAMP` (see Section 3.2 for an explanation of what `SCAMP` does in the GOC Pipeline) are saved to a folder `.\SCAMPed\cluster\filter` so as to keep them separated from the reduced and unreduced images in case something goes wrong in this step of the reduction.

## A4 SWARPing

Next step is using `SWARP` (see Section 3.2 for more detail on this). `reduce.py` first has to change directory into the `.\SCAMPed\cluster\filter` folder from where it can run `SWARP`. Initially this produced highly distorted and noisy images. Attempts were made to change parameters in the configuration files for `SExtractor`, `SCAMP` and `SWARP` to increase the sigma threshold, change the aperture size, reduce the noise but to no success. The issue was found to be caused by entries in the header that represented projection co-efficients that were read by one or all of `SExtractor`, `SCAMP` or `SWARP` which seemed to confuse them as to the location of our images. This further demonstrates the complexities of `FITS` files, their headers and how these interact with software they are put through. As mentioned in Appendix A2, the commented out methods from the code supplied to us caused issues at this stage as these included methods to remove these projection co-efficients.

With the script changed to remove these header entries at the fixing headers stage, `SWARP` could then produce corrected images free of anomalous distortions. This produces `FITS` files with its astrometric solution for our reduced images based on the catalogue produced by `SCAMP`, which is then saved to a folder `.\SWARPed\cluster\filter`. An example of this can be seen in Figure 2 in Section 3.3.

The 4 CCD reduced image paths after `SWARPing` are located in the text file as a list which `SWARP` can read in. This produces a final image called `cluster_filter_FINAL.fit` saved into `.\IMAGES` folder, an example of which can be seen in Figure 3, Section 3.3.

This paper has been typeset from a  $\text{T}_{\text{E}}\text{X}/\text{L}^{\text{A}}\text{T}_{\text{E}}\text{X}$  file prepared by the author.